Air Force Institute of Technology
AFIT Scholar

Theses and Dissertations | Student Graduate Works

6-14-2018

Investigation of Scramjet Flowfield Temperatures at the Boundary Layer with Hyperspectral Imaging

Amy M. Kerst

Follow this and additional works at: https://scholar.afit.edu/etd

Part of the Optics Commons

Recommended Citation

Kerst, Amy M., "Investigation of Scramjet Flowfield Temperatures at the Boundary Layer with Hyperspectral Imaging" (2018). *Theses and Dissertations*. 1758.
https://scholar.afit.edu/etd/1758

This Thesis is brought to you for free and open access by the Student Graduate Works at AFIT Scholar. It has been accepted for inclusion in Theses and Dissertations by an authorized administrator of AFIT Scholar. For more information, please contact richard.mansfield@afit.edu.

www.manaraa.com

INVESTIGATION OF SCRAMJET FLOWFIELD TEMPERATURES AT THE BOUNDARY LAYER WITH HYPERSPECTRAL IMAGING

THESIS

Amy M. Kerst, Civilian

AFIT-ENP-MS-18-J-011

DEPARTMENT OF THE AIR FORCE
AIR UNIVERSITY

AIR FORCE INSTITUTE OF TECHNOLOGY

Wright-Patterson Air Force Base, Ohio

DISTRIBUTION STATEMENT A

APPROVED FOR PUBLIC RELEASE; DISTRIUBUTION UNLIMITED.

www.manaraa.com

The views expressed in this document are those of the author and do not reflect the official policy or position of the United States Air Force, the United States Department of Defense or the United States Government. This material is declared a work of the U.S. Government and is not subject to copyright protection in the United States.

www.manaraa.com

AFIT-ENP-MS-18-J-011

INVESTIGATION OF SCRAMJET FLOWFIELD TEMPERATURES AT THE BOUNDARY LAYER WITH HYPERSPECTRAL IMAGING

THESIS

Presented to the Faculty

Department of Engineering Physics

Graduate School of Engineering and Management

Air Force Institute of Technology

Air University

Air Education and Training Command

in Partial Fulfillment of the Requirements for the

Degree of Master of Science in Optical Sciences and Engineering

Amy M. Kerst, B.S.

Civilian

June 2018

DISTRIBUTION STATEMENT A

APPROVED FOR PUBLIC RELEASE; DISTRIUBUTION UNLIMITED.

www.manaraa.com

AFIT-ENP-MS-18-J-011

INVESTIGATION OF SCRAMJET FLOWFIELD TEMPERATURES AT THE BOUNDARY LAYER WITH HYPERSPECTRAL IMAGING

Amy M. Kerst, B.S.
Civilian

Committee Membership:

Dr. Kevin C. Gross
Chair

Dr. Glen P. Perram
Member

Dr. Michael R. Rhoby
Member

www.manaraa.com

Abstract

Within the domain of chemical propulsion, the fields of combustion diagnostics and computational fluid dynamics each have a long history, and both have led to a better understanding of complex phenomena yielding practical improvements in propulsion systems. As more exotic forms of propulsion are developed, the importance of – and often the challenges with – both diagnostic and simulation capabilities also increase. In the case of scramjet combustion, these challenges primarily arise from the highly turbulent environment in the combustion cavity, and the high-speed, compressible nature of the flowfield. Efforts are underway to develop computer models of scramjet combustion environments to better understand the evolution of the flow field and heat transfer to the walls during combustion. This thesis effort experimentally supports these goals. Specifically, hyperspectral imaging measurements of an optically accessible scramjet were collected for different fueling rates. The primary focus was characterization the magnitude and dynamics of the outer window temperature in its response to combustion of different fueling rate. The outer window temperature was estimated via the radiometric brightness temperature – a quantitative measure of infrared radiant emissions – between 2000 $\text{cm}^{-1} < \tilde{\nu} < 2250\ \text{cm}^{-1}$ where the emissivity of the infrared-grade fused silica window is near unity and atmospheric absorption effects are minimal. Examining the radiant window emissions over a range of frequencies between 2500 $\text{cm}^{-1} < \tilde{\nu} <$4000 cm^{-1}, the spectral region in which the window transitions from opaque to transparent, reveals information related to the temperature gradient normal to the line-of-sight. A simple one-dimensional, numerical heat transfer model is used along with a spectral model for the window to interpret the temporal dynamics of brightness temperature in different spectral bands. Inferring

www.manaraa.com

the actual temperature profile would require temperature-dependent optical properties of fused silica over a broad, high-temperature regime, and at present these are unavailable. This work indicates there would be value in obtaining this optical data so that hyperspectral measurements of the scramjet could be used to quantify heat transfer to the side window. The window represents an important and dynamic boundary condition, and these hyperspectral measurements could be used to validate numerical simulations. Other work in this thesis effort explores qualitative differences in flowfield turbulence under different fueling conditions, and in principle this turbulence characterization could also be used to for comparisons with numerical simulations.

www.manaraa.com

Acknowledgements

A work of this magnitude would not have been possible without assistance and support from many individuals. I am most indebted to my advisor Dr. Kevin Gross for his continual guidance and support of my research efforts, and for making my attendance at AFIT possible. His contributions to my academic and professional life cannot be under emphasized.

I would also like to thank Dr. Michael Rhoby. His previous experience and knowledge, ability to patiently explain difficult concepts, and understanding of how to survive AFIT with one's sanity in tact, played a significant role in my completing this work.

Finally, I would like to thank my soon-to-be husband for his daily support and motivation. I could not have done this without him.

Amy M. Kerst

www.manaraa.com

Table of Contents

Page

Abstract iv

Acknowledgements vi

List of Figures ix

List of Tables xiii

I. Introduction 1

II. Background and Theory 4

2.1 Combustion Diagnostics and Instruments 4
2.1.1 Lasers 4
2.1.2 Infrared Cameras 6
2.1.3 Hyperspectral Detectors 8
2.1.4 Fourier Transform Spectrometers 10
2.2 Interferometric Behavior 13
2.3 Calibration and Instrument Corrections 15
2.3.1 Non-Uniformity Correction 15
2.3.2 Standard Calibration Method 16
2.3.3 Modified Calibration Method 18
2.4 Radiative Transfer 20
2.4.1 Previous Models 21
2.4.2 Current Model – Window Radiance Contributions 24
2.5 Thermal Estimation Methods 27
2.5.1 Brightness Temperature Calculations 27
2.5.2 One Dimensional Thermal Transfer Model 28

III. Experimental Setup and Data Collection 34

3.1 Setup and Instrument Settings 34
3.2 Data Collection 36

IV. Results 38

4.1 Data Representations 38
4.2 Window Surface Brightness Temperature 40
4.2.1 Data Set 1 40
4.2.2 Data Set 2 51
4.3 Brightness Temperatures and Window Transmission Bands 59
4.4 Turbulence and Noise 68

www.manaraa.com

Page

V. Conclusions 74

5.1 Summary of Results 74
5.2 Contributions to Previous and Current Research Efforts 75
5.3 Future Work 77

Bibliography 79

www.manaraa.com

List of Figures

Figure		Page
1	*Left:* Illustration of LIF System. *Right:* Illustration of LAS System. Reproduced with permission from Dr. Rhoby's dissertation. [1]	5
2	Visualization of data stored in a data cube collected by a dispersive spectrometer.	8
3	General concept of dispersive spectrometer set-up.	9
4	*Panel 1:* Imaging Michelson interferometer schematic. *Panel 2:* Collected interferograms and corresponding spectra for two pixels within a scene.	11
5	*Panel 1:* Raw interferogram and spectra for a stable blackbody at 580C. *Panel 2:* Raw interferogram and spectra for measurement of scramjet cavity during combustion.	14
6	Example of image improvement using a non-uniformity correction (NUC)	15
7	Plots of pixel map and spectra for three pixels of the original gain and offset	17
8	Plots of pixel map and spectra for three pixels of the modified gain and offset	19
9	Schematic of the radiative layers used for gas phase modeling of the cavity.	22
10	Plot of spectra from the combustion (purple), cavity metallic elements (green), and free stream above the combustion (red). The black dashed and solid lines show estimates of transmission function at 300°K and 573°K respectively.	23
11	Schematic of the radiative layers used for modeling the radiative effects of the optical viewing window.	25

www.manaraa.com

12 *Left:* Weighting function over window depth for two spectral bands of 2000- 2250 cm^{-1} and 3400- 3800 cm^{-1} respectively. *Right:* Transmission function for the window with the spectral bands of the window marked. 26

13 Plots of weighting function over window depth for a transmissive and opaque spectral band 27

14 Illustration of temperature profiles for 2700°K and 2000°K thermal impulses. Profiles shown before, during and after each burn. A profile is drawn for every three seconds the model is run. 31

15 *Left:* Final temperature profiles after 30 seconds of burning for three consecutive 2700 K thermal impulses. *Right:* Final temperature profiles after 30 seconds of cooling for the thermal impulses shown on the left. 32

16 Setup for hyperspectral imaging of a scramjet cavity 34

17 Schematic of the scramjet cavity. 35

18 Spectrally integrated images for different spectral bands 39

19 Window transmission function showing the spectral band integrated over to examine the outer surface of the window. 40

20 *Left:* Pre-combustion baseline radiance emission from window surface. *Right:* Baseline radiance converted to brightness temperature for window surface. 41

21 Brightness temperature maps of particular times prior, during, and post combustion for consecutive fueling runs. 42

22 Brightness temperature maps of frames taken 1 second post-burn and at the end of the data collection. 44

23 *Top:* Temperature map showing the region averaged over to produce the temperature vs. time plots. *Bottom:* Temperature vs. time for all the fueling runs on an absolute time scale 46

www.manaraa.com

Figure Page

24 Temperature vs. time for all fueling runs, broken time axis 47

25 Temperature vs. time for all fueling runs, broken time axis 48

26 Maximum and minimum temperatures associated with fueling condition 50

27 Brightness temperature of window outer surface prior to, during, and after combustion 52

28 Temperature vs. time for Data Set 2 fueling runs 54

29 Three spatial regions averaged over to produce brightness temperature vs. time plots 57

30 *Left:* Temperature vs. time plots for a spatial region over metal. *Right:* Temperature vs. time plots for a spatial region over the free stream 58

31 Spectral transmission function of the window at two different temperatures. 59

32 Brightness temperature maps for several spectral bands and fueling rates 60

33 Brightness temperatures for different spectral bands 61

34 Spectra generated from the spatial region over the cavity. Taken approximately 0.5 seconds post combustion for each fueling condition 64

35 *Left*: The weighting functions across window depth for each spectral band is displayed. Also plotted is an example temperature profile of the window depth. *Right, Top*: The emission profile of the window generated from the weighting function and the example temperature profile is plotted both in radiance values and brightness temperature. *Right, Bottom*: The transmission function of the window with the five representative spectral bands used for analysis is plotted for reference. 65

www.manaraa.com

36 Comparison of measured spectral emission profiles from the window with model's prediction for the profile. 67

37 Radiance map of a single cube taken in the middle of the burn.Spectral average over 2000-2250 cm^{-1} and 2500-5000 cm^{-1} respectively. 69

38 A raw, time-averaged spectra taken from a single pixel of the data from Data Set 2's 70 sLpm burn 70

39 Maps of the high and low frequency fluctuations in the flame. 72

40 Comparison of high and low frequency fluctuations for all fueling rates 73

www.manaraa.com

List of Tables

Table		Page
1	Predicted Temperature Change at Outer Window Surface	32
2	Predicted Difference in Window Surface Temperature for Successive Impulses	32
3	Fueling Conditions, Parameters	37
4	Average Temperatures for Pre and Postburn Frames, Data Set 1	43
5	Average Temperatures for Postburn Frames	45
6	Minimum and Maximum Window Surface Temperatures for Each Fueling Rate	51
7	Average Temperatures for Pre and Postburn Frames, Data Set 2	53
8	Window Surface Heating Rate for Each Fueling Rate	55

www.manaraa.com

INVESTIGATION OF SCRAMJET FLOWFIELD TEMPERATURES AT THE BOUNDARY LAYER WITH HYPERSPECTRAL IMAGING

I. Introduction

The importance of combustion diagnostics to the advancement of scramjet propulsion systems is significant. Objectives previously accomplished by diagnostic processes include identifying combustion byproducts and their concentrations, temperature distributions, and the velocity and acceleration of flame fronts[2, 3]. Measurement of these parameters enables the design of viable or more efficient systems. Scramjet propulsion is still in development. The advantages resulting from a viable scramjet system to national defense are many. Better understanding of the phenomenology of the combustion cavity through the capture of dependable diagnostic information would significantly contribute to scramjet's continued development.

Accurate characterization of a flame requires acquisition of both chemical and spatial information, and the evolution of these flame characteristics over time. Spectral information leads to the identification of the various species composing the flame through absorption or emission features, and provides insight into these species' concentration levels. Acquisition of spatial information leads to identification of the shape and location of the flame fronts, as well as other variations within the flame. Capture of these data types over time leads to understanding of the progression of the combustion process, flame front fluctuations, and response to condition changes. Ideally, if all this information could be captured simultaneously and continuously, everything about the flame would be known. However, no diagnostic instrument can

www.manaraa.com

currently accomplish simultaneous collection of these data types. Thus, all current methods have strengths and corresponding weaknesses. The environment of a scramjet combustion cavity has additional diagnostic challenges due to the high speed of the flow, large temperature and pressure differentials, and extreme turbulence levels. Thus, diagnostic instruments used to interrogate this environment must overcome or compensate for these challenges in addition to those common to all flame characterization. Recently, imaging Fourier transform spectrometers (IFTS) has been utilized as a diagnostic for scramjet combustion[3]. This work focuses on how the IFTS diagnostic can be used to provide insight into the temperature on the cavity walls. This information would not only lead to a better understanding of the combustion process, but would provide important parameters for computational fluid dynamics (CFD) modeling efforts.

Previous work has been completed evaluating the IFTS instrument's data capture capabilities for flames[4]. Application of the IFTS to the scramjet environment in particular has lead to insights into the chemical species concentrations and distributions[3]. The results of this previous work showed the IFTS diagnostic is capable of contributing valuable information to the current understanding of scramjet flow fields. However, previous results have been limited due to the viewing window – through which the combustion cavity is optically accessible – having a transmission function that transitions from opaque to transparent over the spectral band of diagnostic interest. The effects of the viewing window on gas phase measurements of the combustion was not well understood, and considered a disadvantage to attaining dependable results. This work provides a method by which the variable transmission of the viewing window can be turned to an advantage by analyzing the how different layers along the depth of the widow contribute to the total measured radiance, and

www.manaraa.com

connecting these to temperature.

Within the background, a summary of diagnostic methods currently used to analyze combustion environments is provided, with brief summaries of their strengths and weaknesses. Following this, an explanation of calibration methods and data processing techniques is given. A unique calibration process was developed, as the lower calibration point was taken from a non-uniform source. The process used to overcome this challenge is described in detail. Finally, the models for radiative transfer and thermal heat transfer are developed, and later used to provide insight and context to the reported results.

These combined results provide additional information and perspective to current knowledge of scramjet combustion cavities, adding to the information required to create a viable computational fluid dynamics model of the scramjet combustion environment. Furthermore, the IFTS is show to have values as a diagnostic for the examination of highly turbulent scenes.

www.manaraa.com

II. Background and Theory

2.1 Combustion Diagnostics and Instruments

A review of instruments commonly employed in combustion diagnostics will allow for an appropriate literature review, and an understanding of current limitations in the field. Three broad categories of methods will be considered: lasers, infrared cameras, and hyperspectral instruments. More particular methods will be mentioned in each section, as well as a summary of their strengths and weaknesses.

2.1.1 Lasers

The dominant diagnostic technique in combustion analysis is laser spectroscopy[5, 6]. Many different kinds of laser methods have been developed, three of the most notable methods being Laser Absorption Spectrometry (LAS)[7, 8, 9], Laser Induced Florescence (LIF)[10, 11, 12, 13], and Coherent Anti-Stokes Raman Scattering (CARS)[14]. The full details of these methods and their applications are not addressed here, and the reader is encouraged to reference the literature for further detail. There are several reasons laser methods are favored in combustion diagnostics, including high spectral resolution and collection speed. A general overview of methodology for LIF, LAS, and CARS measurements will be considered here, as other laser methods frequently exploit the principles of these three methods.

Considering first LAS, this method utilizes principles corresponding to absorption to interrogate a flame, and a simple diagram of the process is shown in the left image of Figure 1. A laser beam is tuned to wavelengths corresponding to the absorption band of the element of interest in the flame. A sensor is placed on the opposite side of the flame, in the path of the laser beam. Since the initial intensity of the beam is know, the attenuation of the beam can be measured and from this, elements of

www.manaraa.com

interest can be detected. Similarly, LIF, shown in the right image in Figure 1 uses a tunable laser beam set to absorption bands of interest to interrogate the flame, however, the detector is placed perpendicular to the direction of beam propagation. Thus, the detector collects the emitted florescence from the excited states relaxing back into their lower states.

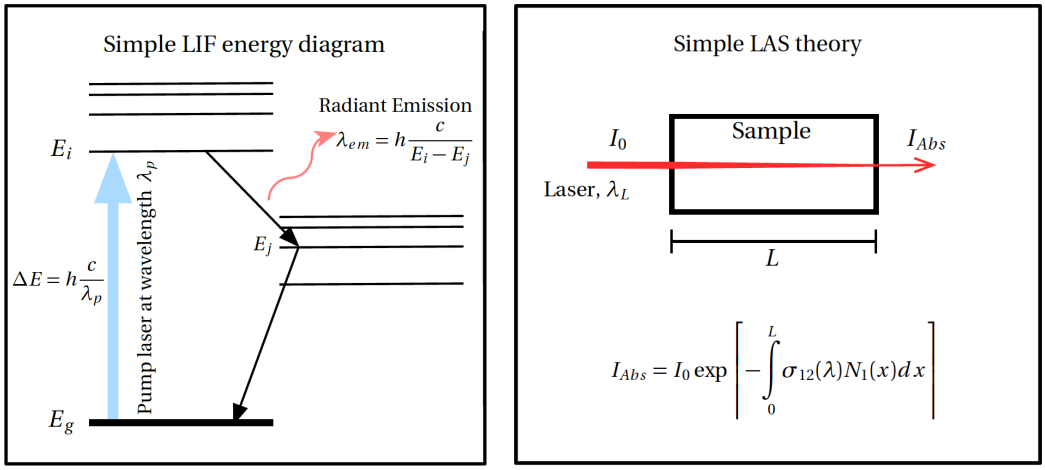

Figure 1. ***Left:*** **Illustration of LIF System.** ***Right:*** **Illustration of LAS System. Reproduced with permission from Dr. Rhoby's dissertation.** [1]

Weaker signals are often better detected using LIF methods, as the signal is positively biased from the background signal instead of negatively biased. However, the setup for LAS systems tend to be slightly less labour intensive.

CARS exploits physical principles bearing similarity to LIF. However instead of a particle being excited from a lower state to a higher one, then decaying back to a lower state, the particles transition through virtual states. These virtual states exist continuously in an atomic system, and novel information about the particle can be collected by comparison of relative emission intensities. Many measurement techniques using variations of these principles exist, and contribute valuable information to the field.

The advantages of laser systems for flame interrogation are many. The collection

www.manaraa.com

time steps for these systems are limited only by the speed of the detector, thus fluctuations in the flame are captured with a high level of accuracy. Furthermore, the spectral resolution of these systems is very fine, being primarily limited by the number of steps used at the laser wavelengths are moved through its tunable range. Theses systems can be expanded to two dimensions by using a laser plane, as in planar LIF (PLIF), and a focal plane array in place of a detector. Laser systems many advantages are offset by the complexity and precision required for setup, and subtleties involved in data collection and interpretation. For example, as a tunable laser beam is moved through its range of wavelengths, the output intensity of the beam varies. This variation is not desirable, as the initial output of the laser beam must be known to accurately interpret the data signal. These challenges are overcome through use of additional detectors, and beam modulation techniques such as lock-in amplifiers. Each of these additions adds layers of complexity to the detection system. There are also some inherent limitations for laser systems. First, the spectroscopic range is very limited, due to the fact only a small range of wavelengths can be tested at a time. Second, the spatial information that can be captured instantaneously is limited to the size and shape of the beam. Increasing the size of the beam can lead to complications. Since the interrogation method is active, using beam inputs over a large spatial range risks cross interactions in energy transitions, which would ultimately corrupt the resulting output.

2.1.2 Infrared Cameras

Infrared cameras are used widely for a variety of applications including characterizing thermal radiation of solids, remote sensing, and combustion diagnostics.[15, 16, 17, 18, 19, 20, 21] Their particular uses with regard to flames arise from their ability

www.manaraa.com

to rapidly collect images with a high level of spatial resolution. This capability is particularly useful for determining flame velocity and the evolution of flame fronts.

Data capture for IR cameras is relatively simple, as it is a passive "point and shoot" system. Setup considerations are limited to instrument field of view (FOV), and radiative transfer though intermediate elements, such as the atmosphere. Once the photons reach the camera, an optical system focuses the radiance onto a focal plane array (FPA). The incident photons are then converted to a digital number. Given an appropriate calibration using a uniform radiance source, these digital numbers can then be converted to a radiance value. Each pixel in the FPA see a limited region or field of view (FOV) and the spectral bandwidth of the focal plane array (FPA). Thus, the pixel value can be connected to a particular spatial area along a line-of-sight, and therefore the radiance value to the line of sight contributions from that region. The rapidity of the image capture enables much information to be gained on the flame's shape, velocity, and temperature fluctuations over time.

Infrared imagers also have limitations. First, the spectral information will be averaged into a single radiance value in the form of the pixel's output. The amount of averaging can be limited by using a narrow spectral filter. For example, if a filter were put on a camera that only allowed light to reach the camera from a limited spectral range, one could draw conclusion about what is in the scene based on what materials are know to emit or absorb in that particular band. However, this again limits one to looking at a very narrow spectral band, and no information about the spectral variation over the band can be acquired. Second, imagers average over the third spatial dimension. The radiance collected by the FPA is is a line of sight average. Thus, imagers offer a high level of spatial information about the flame's behavior, but are severely limited in their ability to provide high level spectral information.

www.manaraa.com

2.1.3 Hyperspectral Detectors

2.1.3.1 Dispersive Spectrometers

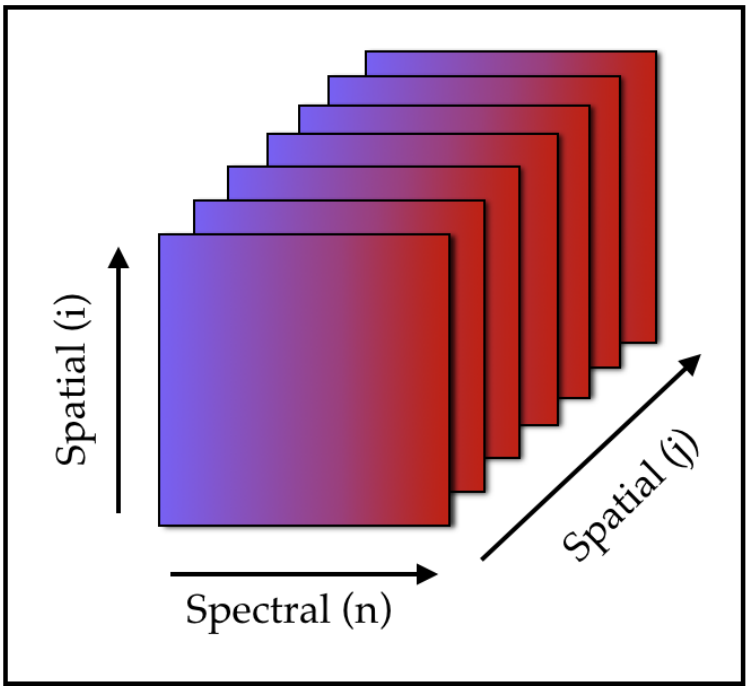

Figure 2. Visualization of data stored in a data cube collected by a dispersive spectrometer.

Efforts to overcome the limited spectral range or resolution of the two previous diagnostic techniques has led to hyperspectral detectors to be used in combustion diagnostics[1, 22, 23, 24]. Many of these systems are capable of capturing highly resolved spectral data over a continuous wavelength range of up to several microns. Furthermore, many systems also have imaging capabilities and are able to collect up to two dimensions of spatial information. Two common methods of hyperspectral detection are dispersive spectrometers and Fourier transform spectrometers. A dispersive spectrometer depends on some optical element, usually a prism or a grating, to separate the source light into the composing wavelengths. The general method by which this is accomplished is shown in Figure 3. The incoming light is focused

www.manaraa.com

through imaging optics down to a slit. The slit ensures that the light is coherent and coming from a small spatial location within the scene. After passing through the slit, the light is collimated onto a dispersive element. If this element is a prism, the wavelength dependent index of refraction, $n(\lambda)$, will cause each wavelength to bend by a different amount. As a result, the different wavelengths will be focused on unique locations on the focal plane array. If the dispersive element is a grating, the end result is the same, but dispersion occurs by using a periodic structure to scatter the light by different amounts instead of bending it. To create a 3D image with a spectral and two spatial dimensions, the FOV of the instrument must be scanned across the 2D image space, and stored in either a dimension of the FPA, or in a separate frame. Figure 2 illustrates the way this is done. The spectral information for a particular

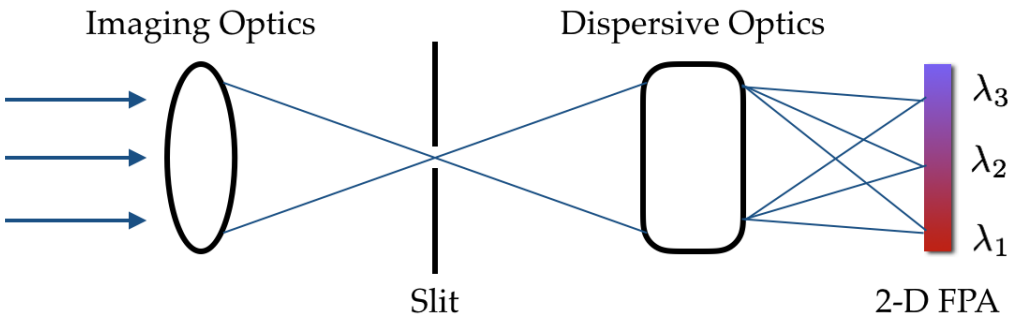

Figure 3. General concept of dispersive spectrometer set-up.

location in the scene is stored in the n^{th} dimension of the FPA. As the FOV moves across one spatial dimension of the scene, the light moves up the FPA creating bands of varying intensity depending on the spatial location. As the FOV moves across the second spatial dimension, a new frame is used and the previously described process repeated. The resolving power of these systems is dependent on both the slit width, as it determines the level of coherence in the incoming light beam, and the material properties of the dispersive element. The spectral band-width is determined by

www.manaraa.com

the resolving power, and the size of the FPA. Band-widths of multiple microns and resolution of a few nanometers is possible. With this system, broad band spectral data can be captured and connected to a particular location within the scene. This has potential to give much greater insight into the behavior of the flame as a whole. However, since the spatial information is collected over time, we cannot gain an instantaneous image of the spectral behavior of the flame at all locations. Some kind of averaging must be done to interpret the data in a universal fashion.

2.1.4 Fourier Transform Spectrometers

Fourier transform spectrometers collect hyperspectral data arrays by modulating the incoming radiation, then taking the Fourier transform of the captured interference patterns. By far the most common method for radiation modulation in these systems is by use of a Michelson interferometer. This is the method used in our diagnostic instrument, and therefore will be covered in detail.

A Michelson interferometer is capable of collecting broad-band spectral information while maintaining spectral resolutions ranging from over 100 cm^{-1} to less than 1 cm^{-1}. The interferometer is combined either with a detector, if it is nonimaging, or a focal plane array (FPA) if it is an imager. Here, the imager will be considered, since the non-imager can be thought of as a FPA system with one pixel. When the interferometer is combined with a FPA, the combined system is known as an imaging Fourier transform spectrometer (IFTS), and can provide insight into the broad-band spectral behavior of a scene at particular locations over time.

A Michelson interferometer collects spectral information by measuring the interference patterns of incoming radiation. Taking the Fourier transform of these interferograms yields information-rich spectra. A schematic of the Michelson system and resulting data is shown in Figure 4. Incoming radiation from the scene is split

www.manaraa.com

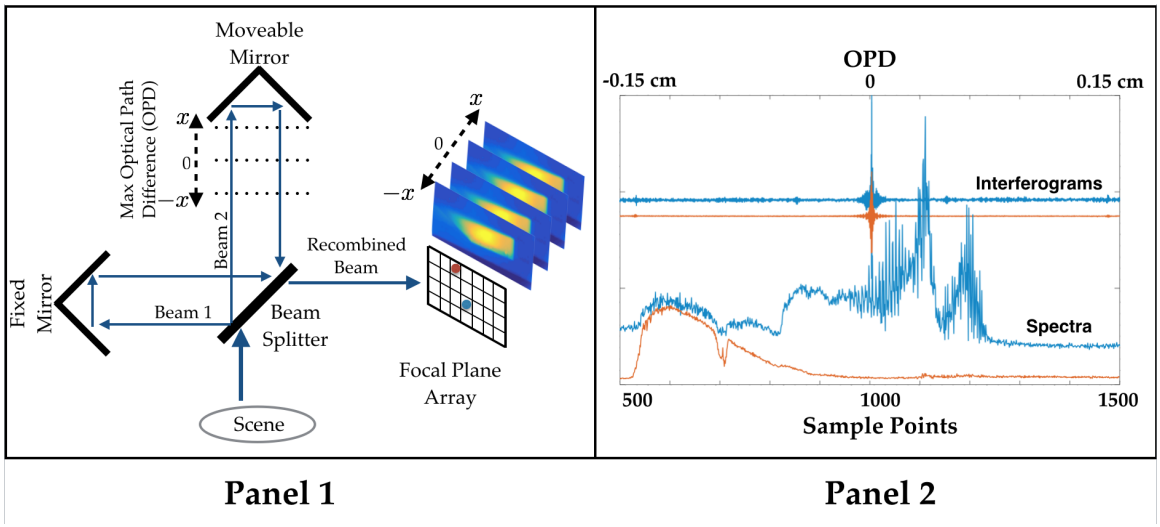

Figure 4. ***Panel 1:*** **Imaging Michelson interferometer schematic.** ***Panel 2:*** **Collected interferograms and corresponding spectra for two pixels within a scene.**

into two beams which are then reflected off of two mirrors – one stationary and one movable – imposing an optical path difference (OPD) between the beams. The two beams are then recombined and focused onto a focal plane array (FPA). A single interferogram is produced for each pixel when the moveable mirror is scanned through the OPD range. The continuous broadband information is acquired by recording interference patterns from scene radiance of all wavelengths, and the limiting factor on the bandwidth is the spectral responsivity of the instrument's detector. The spectral resolution is varied by changing the maximum OPD of the mirror sweep. Thus, the primary limiting factor on the resolution of the Michelson system is the maximum OPD or scan length that the system can attain.

When the recombined radiation is focused onto a FPA, interferograms will be generated at each pixel. The resulting individual spectra will then correspond to the line-of-sight (LOS) integrated radiance of a particular spatial location within the scene. An image is captured for each sample point of the movable mirror over the full OPD. The series of images generated over a full scan compose a single data cube, and contains a single broadband spectra for each pixel of the FPA. The time required to

www.manaraa.com

generate a single data cube is dependent on both the spectral and spatial resolution, thus higher resolutions require a longer collection time.

The output interferogram $I(x)$ for some pixel i can be characterized by Equation 1

$$I_{ij}(x,\tilde{\nu}) = \int_0^\infty (1+\cos(2\pi\tilde{\nu}x))G_{ij}(\tilde{\nu})(L_{ij}^S(\tilde{\nu}) + L_{ij}^I(\tilde{\nu}))d\tilde{\nu} = I_{ij}^{DC}(\tilde{\nu}) + I_{ij}^{AC}(x) \quad (1)$$

where $L_i^S(\tilde{\nu})$ and $L_i^I(\tilde{\nu})$ represent scene radiance and instrument self-emission, respectively. The term $(1+\cos(2\pi\tilde{\nu}x))$ accounts for the modulation of the Michelson interferometer, and $G_i(\tilde{\nu})$ is the system response function. Note that the output interferogram $I(x)$ could be represented as a function of either mirror position x or of time t into the scan, as these two variables are related by the mirror velocity v. A two point calibration using blackbodies[25] is utilized to find the system response and self-emission for each pixel. The temperatures of the blackbodies are chosen to produce radiance values above and below the range of scene output radiances, and close enough to the scene values to assume a linear system response function.

The output $I(x)$ can be separated into the terms I^{DC} and $I^{AC}(x)$. The I^{DC} term provides the spectrally integrated intensity from the scene, while the $I^{AC}(x)$ term is the cosine transform of the spectrum produced by the modulation of the Michelson. If the scene has significant turbulence-induced radiance fluctuations during the collection of a data cube, the DC piece becomes time-dependent and coupled to the AC component. This coupling considerably complicates analysis and interpretation, but through a previously developed method for averaging the data ensemble meaningful interpretation is possible[4, 3]. The time dependance of the I^{DC} will be used to qualitatively visualize turbulent intensity fluctuations throughout the cavity and understand the influence of turbulence on window temperature estimations.

www.manaraa.com

2.2 Interferometric Behavior

When the Fourier transform of a signal is taken, the signal is decomposed into its frequencies contributing to the total signal. For a Fourier transform spectrometer, the fundamental frequencies of the decomposed signal are gathered from the interference patterns of the radiation incident on the sensor. For the IFTS system, signal frequencies are contributed both by the wavelengths of the radiation and fluctuations within the scene. The range of radiation frequencies captured depends on the spectral range of the instrument. Scene fluctuation frequencies, however, can be captured over the entire frequency range the instrument is capable of resolving – from approximately 3.33 cm^{-1} to the Nyquist frequency of 7900 cm^{-1} for IFTS system used in this work. This range is directly dependent on the spacing between the mirror's sample points. The capture of scene fluctuation is better illustrated by rewriting Equation 1 as time dependent as shown in Equation 2

$$I_{ij}(vt,\tilde{\nu}) = \int_0^\infty (1+\cos(2\pi\tilde{\nu}vt))G_{ij}(\tilde{\nu})(L_{ij}^S(\tilde{\nu},t)+L_{ij}^I(\tilde{\nu}))d\tilde{\nu} = I_{ij}^{DC}(\tilde{\nu},t)+I_{ij}^{AC}(v,t) \tag{2}$$

were v is the velocity of the Michelson's movable mirror. This now shows that there is time dependent variation contributed to the interferogram by the frequencies at which the scene fluctuates. When scene fluctuations are added to the interferometric signal, the AC component of the interferogram is no longer only influenced by radiance contributions from the scene, but also the scene's modulation frequencies. The manner in which the signal changes with the addition of scene fluctuation are further illustrated in Figure 5 where the interferograms and spectra from a stable and unstable scene are contrasted. Data capture in relation to time, mirror OPD, mirror frequency, and spectral wavenumbers are all represented. When the scene is stable, the composing signal frequencies come from the interference patterns of the

www.manaraa.com

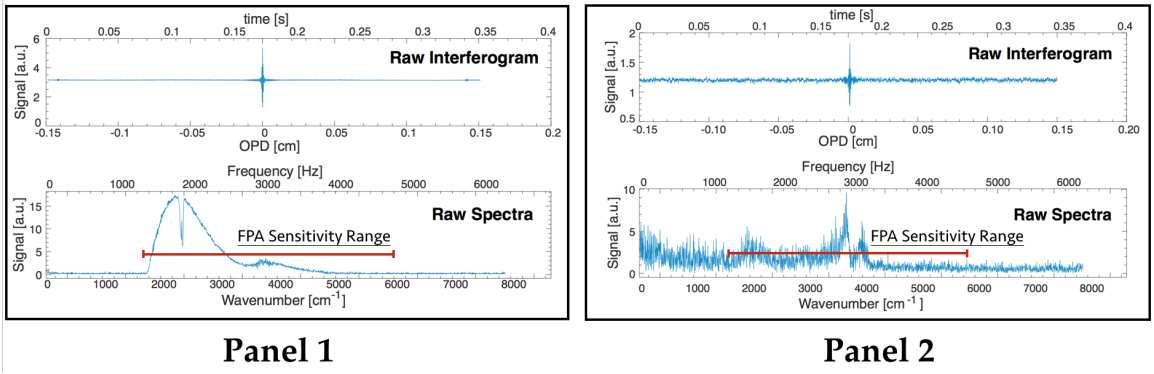

Figure 5. ***Panel 1:*** **Raw interferogram and spectra for a stable blackbody at 580C.** ***Panel 2:*** **Raw interferogram and spectra for measurement of scramjet cavity during combustion.**

incident radiance only. In contrast, if the scene is fluctuating, the scene variation frequencies will appear over the entire frequency range the instrument is capable of resolving; from 3.33 cm^{-1} to the Nyquist frequency of 7900 cm^{-1}. The FPA is sensitive to the radiation in the 1750 - 6000 cm^{-1} range, thus in this band, signal can be contributed by both scene radiance and fluctuations. This is illustrated in panel 1 of Figure 5 where the scene fluctuation appears as noise riding on the spectral features arising from scene radiance. Outside the FPA's sensitivity range, however, it can be concluded that any recorded signal will have arisen solely from scene fluctuation. Again referring to panel 1 of Figure 5, significant signal levels were recorded above and below the instrument bandpass. Insight into scene fluctuation can be gained by band-averaging the signal on either side of the camera bandpass. The range below the camera bandpass corresponding to lower frequency scene fluctuations, and the range above the bandpass to high frequency scene fluctuations. Since an interferograms are captured for every pixel, we can connect scene fluctuation to particular spatial locations, and create a map of the of the low and high frequency scene variations.

www.manaraa.com

2.3 Calibration and Instrument Corrections

Two kinds of correction methods were used for initial processing of the data. The first is an instrument non-uniformity correction used to remove instrument effects for better observation of the raw data used to show scene turbulence. The second is a two point calibration using two blackbodies to convert the raw recorded spectra to spectra in apparent radiance units through the determination of spectral gain and offset for the instrument. Ideally, this two point calibration is a straight forward, well defined process[25]. However, due to defects in one of the calibration sources, a modified calibration method was developed and applied to the data reported in this work. The the instrument non-uniformity correction, the standard two point calibration method, and the modified method will all be explained in the subsequent sections.

2.3.1 Non-Uniformity Correction

Corrections to the turbulence data captured outside of the camera bandpass were done with a one point non-uniformity correction. The effect of this method is illustrated in the contrast between the two images in Figure 6. Since the turbulence signal

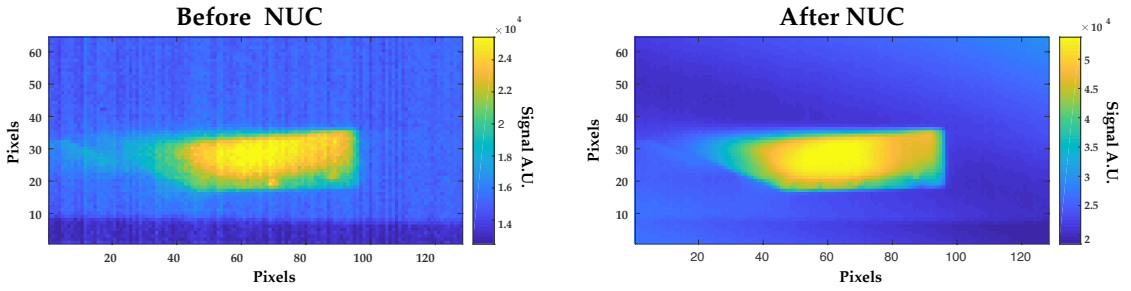

Figure 6. Example of image improvement using a non-uniformity correction (NUC)

cannot be converted to meaningful, physical units, it is left in raw instrument spectra.

www.manaraa.com

Thus, for display of this data, the objective was to removed the instrument artifacts and non-uniformity between individual pixels. To accomplish this, a single uniform blackbody source was measured, and a gain and offset were extracted by considering two different spectral bands. Since the source was known to be uniform, any variation in the recorded image is assumed to be a result of material non-uniformity from pixel to pixel. These non-uniformities were corrected by assigning some correction coefficient m_{ij} to each of the pixel's responds values. The offsets were calculated and applied for each individual frame composing a cube in the turbulence data. This was done to ensure that the interference effects caused by each frame's unique OPD would be mitigated. When these corrections applied across all pixel's raw responds values, the scene was corrected to a uniform value. To ensure instrument artifacts were eliminated as effectively as possible, this pixel-by-pixel correction was calculated The variation in the pixel responds was assumed to be spectrally independent.

2.3.2 Standard Calibration Method

The upper and lower calibration points for a two point spectral calibration are chosen such that the system response is linear over the chosen spectral range. Assuming this linear response, the relation between raw spectra and measured radiance can be written as in Equation 3.

$$Y_{ij}(\tilde{\nu}) = G_{ij}(\tilde{\nu})(B(T_k, \tilde{\nu}) + L^I_{ij}(\tilde{\nu})) \tag{3}$$

where for each pixel ij, $Y_{ij}(\tilde{\nu})$ is the raw spectra, $G_{ij}(\tilde{\nu})$ is the spectrally dependent instrument gain, $B(T_k, \tilde{\nu})$ is the radiance emission from a uniform blackbody at temperature T_k, and $L^I_{ij}(\tilde{\nu})$ is the instrument self-emission. When the right-hand side of Equation 3 is expanded, the raw spectra can be expressed in terms of a spectral gain

www.manaraa.com

and offset, as shown in Equation 4

$$Y_{ij}(\tilde{\nu}) = G_{ij}(\tilde{\nu})B(T_k, \tilde{\nu}) + O_{ij}(\tilde{\nu}) \tag{4}$$

These gain and offset terms can be solved for by measuring the raw spectra for two uniform blackbody source where the spectral profile is known. This gain and offset can than be used to convert the raw spectra of an unknown source.

Ideally, the method just described would have been used to create a spectral calibration. Unfortunately, a defect in the low temperature cavity blackbody source caused a poor gain and offset to be calculated using this method. Figures 7 show plots of the spectrally averaged gain $G_{ij}(\tilde{\nu})$ and offset $O_{ij}(\tilde{\nu})$ across the pixels and the spectra of the gain and offset for three select pixels. From these plots it is evident that the

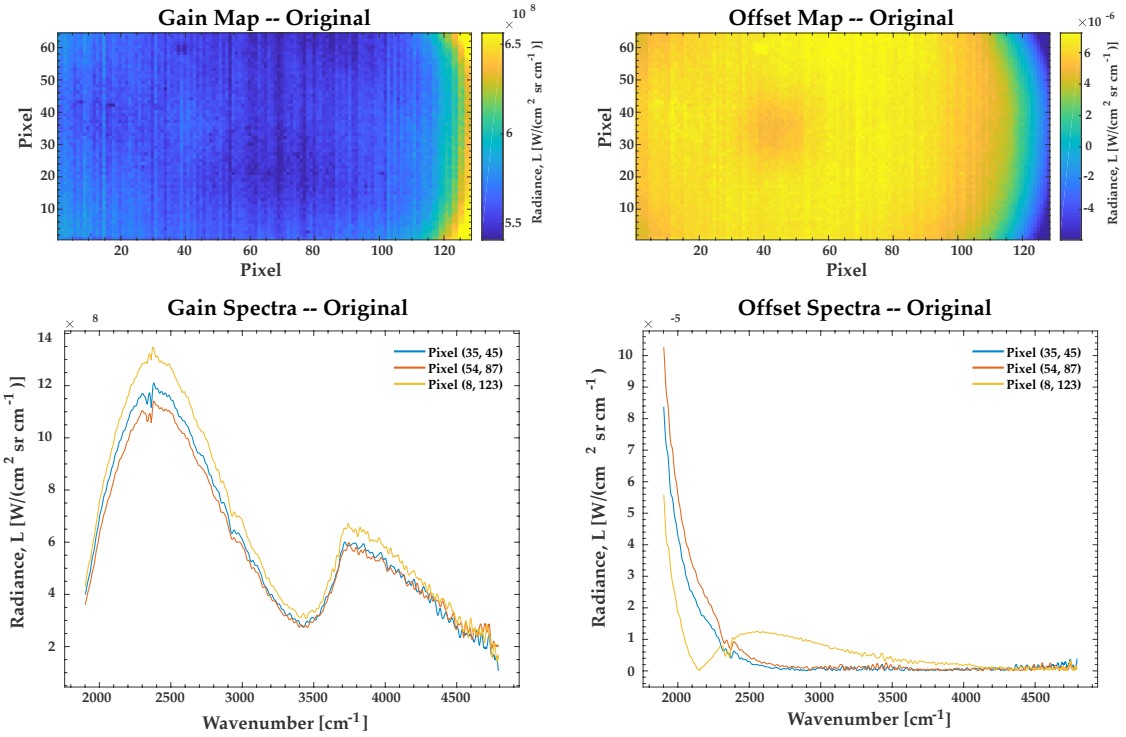

Figure 7. Plots of pixel map and spectra for three pixels of the original gain and offset

www.manaraa.com

center of the cavity blackbody had a region of lower emissivity in the center of the cavity. Furthermore, it appears that the blackbody did not perfectly fill the field of view, producing edge effects. These non-uniformities from the cavity blackbody are being carried through to the calibration offset, corrupting it. The defects were corrected using the modified calibration method detailed in the next section.

2.3.3 Modified Calibration Method

Development of a modified calibration method to correct for the errors produced by the standard method was accomplish and is described in this section. First, however, several assumptions made about the instrument than influence this method's development must be stated. First, it is assumed that the only source of variation in instrument response from pixel to pixel is caused by material variations in the focal plane array, and has no spectral or temperature dependence. Second, since the instrument temperature never exceeds 47°C, in spectral regions beyond 3500 cm^{-1} it can be assumed that the self-emission is negligible and thus falls to zero. Taking these assumptions, Equation 3 can be rewritten in the following form

$$Y_{ij}(\tilde{\nu}) = m_{ij}g(\tilde{\nu})B(\tilde{\nu}, T_k) + m_{ij}g(\tilde{\nu})L_{self}(\tilde{\nu}, T_{self}) \tag{5}$$

where $G(\tilde{\nu})$ is the instrument gain, $B(\tilde{\nu}, T_k)$ is the spectral radiance from some uniform blackbody source, $L_{self}(\tilde{\nu}, T_{self})$ is the instrument self-emission, and the coefficients m_{ij} are the relative pixel response. The method for solving for the corrected gain $G(\tilde{\nu})$ and offset $O_{ij}(\tilde{\nu})$ is as follows. The terms m_{ij} were calculated using the one point non-uniformity correction described in the first section. The term $g(\tilde{\nu})$ was found first by considering the spectral region beyond 3500 cm^{-1} where the self-emission $L_{self}(\tilde{\nu}, T_{self})$ is negligible and assumed to be zero, and the second term in Equation 5 drops out. Inserting the high temperature source radiance – which was

www.manaraa.com

truly uniform – for $B(\tilde{\nu}, T_k)$, a solution for $g(\tilde{\nu})$ was found for the spectral band beyond 3500 cm^{-1}. Following this, $g(\tilde{\nu})$ was solved for in the spectral band below 3500 cm^{-1} by using an ideal blackbody emission profile for $L_{self}(\tilde{\nu}, T_{self})$, and selecting a subset of pixel's $Y_{ij}(\tilde{\nu})$ that were believed to record emissions closest to the true blackbody profile. The selection of this subset of pixels was accomplished by first eliminating the pixels which were clearly capturing defects, such as the edges of the cavity and its center. Elimination of the less obvious error regions and further refining the subset was accomplished by selecting the brightest 10% of pixels in the 3500 – 5000 cm^{-1} spectral band. This subset of pixels was chosen as the best representation of the lower temperature blackbody radiation. These values were then substituted for the $Y_{ij}(\tilde{\nu})$ values, along with the lower blackbody's ideal emission profile $B(\tilde{\nu}, T_k)$, and a solution for $g(\tilde{\nu})$ was found for the lower spectral range.

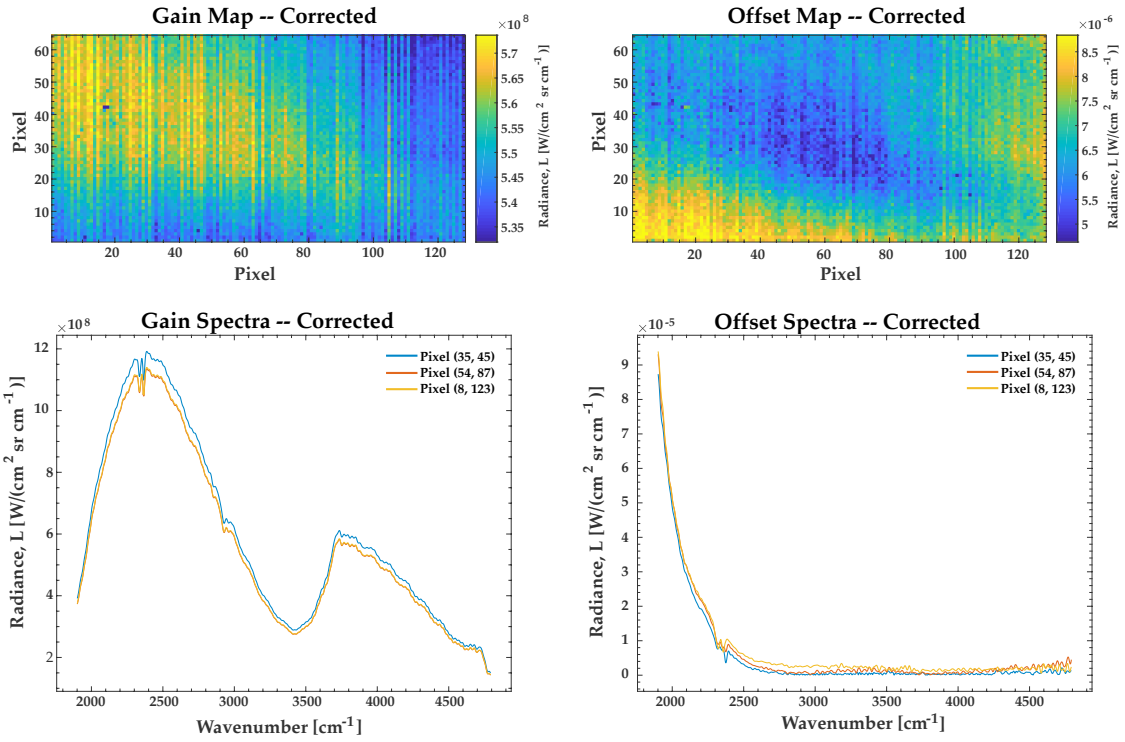

Figure 8. Plots of pixel map and spectra for three pixels of the modified gain and offset

www.manaraa.com

Taking these solutions for $g(\tilde{\nu})$ and combining them, we are again able to write the calibration in form giving in Equation 4. The corrected gain $G(\tilde{\nu})$ and offset $O_{ij}(\tilde{\nu})$ using this method are shown in Figure 8. Notice that the structure and spectral anomalies evident previously in Figure 7 has been removed in Figure 8 has been removed, thus eliminating artifacts from the calibrated data. This modified calibration was used in the results reported in this work.

2.4 Radiative Transfer

Every physical body can absorb, reflect, or transmit radiation. The radiative characteristics of an object will depend on its temperature, optical properties, and the contributing radiance of the objects in the immediate surroundings. These principles can be used to gain insight into the physical parameters of a material or series of materials within the field of view (FOV) of a sensor. For a material, the primary radiative properties will be the absorbance, α, reflectivity, ρ, and transmissivity τ. For some radiance incident on some material, the effect on the total radiance will be distributed between these three optical processes. This relationship is expressed in Equation 6

$$1 = \alpha(\tilde{\nu}, T) + \rho(\tilde{\nu}, T) + \tau(\tilde{\nu}, T) \tag{6}$$

Note that the α, ρ, and τ for a particular material will vary both with wavenumber, $\tilde{\nu}$ and the temperature of the material, T. Thus, depending on the spectral band of interest, the effect of a particular material on the total measured radiance may vary. The quantity, α, can also be expressed in terms of emissivity ϵ, which is the fraction of radiation thermally emitted relative to a blackbody at the same temperature. This relationship is expressed in Equation 7

$$\alpha(\tilde{\nu}, T) = \epsilon(\tilde{\nu}, T) \tag{7}$$

www.manaraa.com

For the cases treated in this work, scattering effects are assumed to be negligible as the radiance is assumed to be perpendicularly incident on any material encountered while traveling over some path length s. Thus, the total radiance transmitted through some path length s' to s for a one-dimensional, non-scattering scene can be written as shown in Equation 8

$$L(\tilde{\nu}) = L_0(\tilde{\nu})e^{-\int_0^l k_a(\tilde{\nu},s)ds} + \int_0^l k_a(\tilde{\nu},s)B(\tilde{\nu},T(s))e^{-\int_s^l k_a(\tilde{\nu},s')ds'}ds \tag{8}$$

where $k_a(\tilde{\nu}, s'')$ is the wavelength-dependent absorption (a) coefficient which depends on the local optical properties at a point s'', and $B(\tilde{\nu}, T)$ is Planck's distribution function at the local temperature $T(s'')$, and $L_0(\tilde{\nu})$ is the background radiation. For a gas undergoing combustion, the optical properties are τ, α and ϵ and are dependent on the molecular concentration and composition of the gas. Note that the exponential term in Equation 8 is the transmission function $\tau(\tilde{\nu}, s', s)$ for some path length calculated using Beer's law.

$$\tau(\tilde{\nu}, s', s) = e^{-\int_{s'}^{s} k_a(\tilde{\nu},s'')ds''} \tag{9}$$

These fundamental principles of radiative transfer provide the basis on which simplified models were developed to describe the radiometric behavior of the combustion cavity. The following sections describe models used in previous work, as well as the model developed for this work.

2.4.1 Previous Models

Previous work was completed using the IFTS to explore the chemical species concentrations and distributions of the flame, as well as temperature profiles.[3] In that research, a model was developed for the total radiance emitted from the cavity, where

www.manaraa.com

solids and gases are in sequence, approximating the scene as a system of homogenous layers. The discretized solution to the radiative transfer problem through n homogenous layers is given by:

$$L(\tilde{\nu}) = L_0 \prod_{i=0}^{n} \tau_i(\tilde{\nu}, T) + \sum_{i=0}^{n} (B(\tilde{\nu}, T_i)(1 - \tau_i(\tilde{\nu}, T)) \prod_{j=i+1}^{n} \tau_j(\tilde{\nu}, T)) \tag{10}$$

where L_0 is the background radiation, $\tau_i(\tilde{\nu}, T)$ is the temperature dependent transmission function for each layer, and $B(\tilde{\nu}, T_i)$ is the blackbody radiation profile for temperature of layer i. A schematic of the radiative layers used in the gas phase models is provided in Figure 9. Efforts to model the spectra of the gaseous byprod-

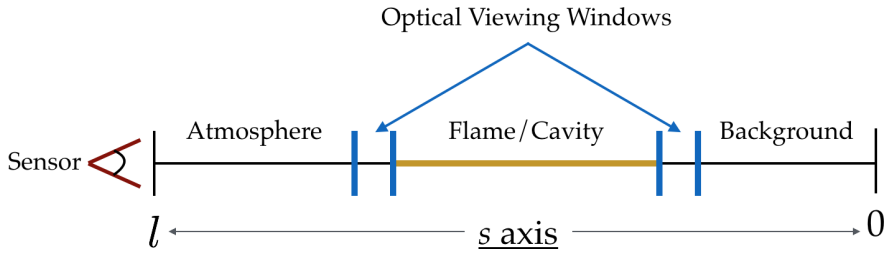

Figure 9. Schematic of the radiative layers used for gas phase modeling of the cavity.

ucts of the cavity were very promising, and excellent agreement between theory and data were obtained. However, confidence in these results was undermined by lack of dependable knowledge of the fused silica window's transmission function at high temperatures. Estimates for the window transmission function $\tau_w(\tilde{\nu})$ are not currently available for temperatures exceeding 573°K. Figure 10 shows spectra from the cavity plotted with the best estimates for $\tau_w(\tilde{\nu})$ at room temperature and 573°K, illustrating the spectral regions where fitting the spectra would provide poor results due to window effects. Since $\tau_w(\tilde{\nu})$ is temperature dependent and the combustion temperatures of the gas are known to exceed 2000°K these transmission function estimates were

www.manaraa.com

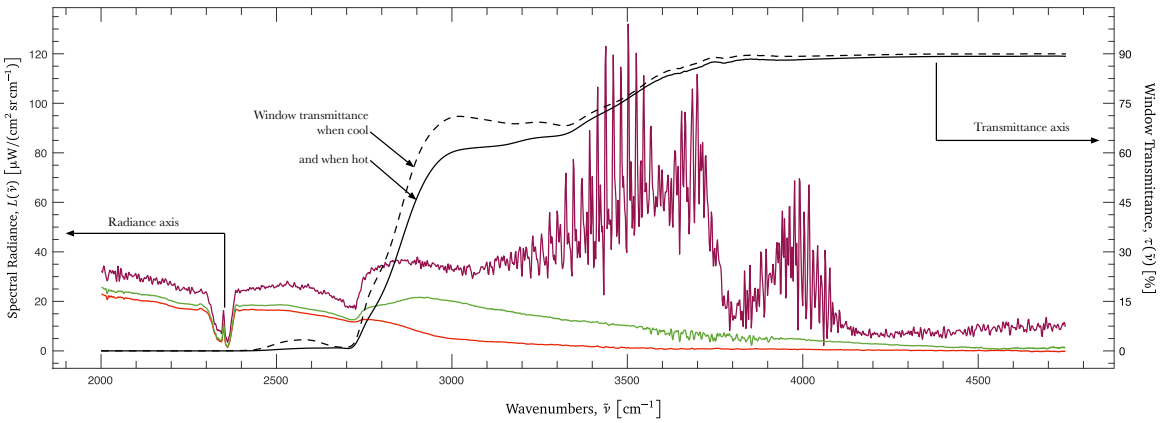

Figure 10. Plot of spectra from the combustion (purple), cavity metallic elements (green), and free stream above the combustion (red). The black dashed and solid lines show estimates of transmission function at 300°K and 573°K respectively.

not considered highly dependable. Efforts proceeded by only fitting the spectra in a band where $\tau_w(\tilde{\nu})$ was above 80%, or in spectral bands beyond 3100cm^{-1}, where it was assumed that any absorption effects could be treated as a baseline shift. The results gained using this methodology attained good agreement with current theory and provided additional insight into the scramjet combustion process. The reader is encouraged to consult the literature for a full treatment of these results.[3]

The work previously completed would benefit from better knowledge of the window effects, and the results could be studied with greater confidence in their dependability. Thus the radiative models developed for this work focus on better understanding the effects of the window over the spectral bands disregarded previously. In the process of gain correct knowledge of the window effects, it became evident that the window's behavior could be exploited to gain a better understanding of thermal heat transfer through the window. Development of models used for this purpose are presented in the next section.

www.manaraa.com

2.4.2 Current Model – Window Radiance Contributions

Recall the discretized solution of radiative transfer through n homogenous layers provided in Equation 10. As the transmittance function of the outermost layer approaches zero, Equation 10 will simplify to

$$L(\tilde{\nu}) = \tau_{atm}(\tilde{\nu})B(\tilde{\nu}, T_w) \tag{11}$$

where τ_{atm} is the transmission of the atmosphere between the window and camera, and $B(\tilde{\nu}, T_w)$ is the planckian function at the temperature of the outside of the window, T_w. As τ_w increases, larger amounts of radiation are transmitted, first from the interior layers of the window, then from the cavity and other background elements. Thus, as the window becomes transparent, Equation 10 is an appropriate expression for the total radiance.

Focusing primarily on the transmittance and emission of the window, if the window is discretized in some s infinitesimal layers, and the radiance against the inside of the window from the cavity is considered as some homogenous contribution L_0, then we can rewrite Equation 8 in the following form

$$L(\tilde{\nu}) = L_0 e^{-\int_0^l k_w(\tilde{\nu},s)ds} + \int_0^l B(\tilde{\nu}, T(s))W(\tilde{\nu}, s)ds \tag{12}$$

where $W(\tilde{\nu}, s)$ is the weighting function for the radiance contributions from some window layer s. Note that mathematical form of this weighting function is

$$W(\tilde{\nu}, s) = k_w(\tilde{\nu}, s)e^{-\int_s^l k_w(\tilde{\nu},s')ds'} \tag{13}$$

A schematic of the radiative layers used in this model is provided in Figure 11.

The formulation for the total detected radiance in Equation 12 is enlightening as

www.manaraa.com

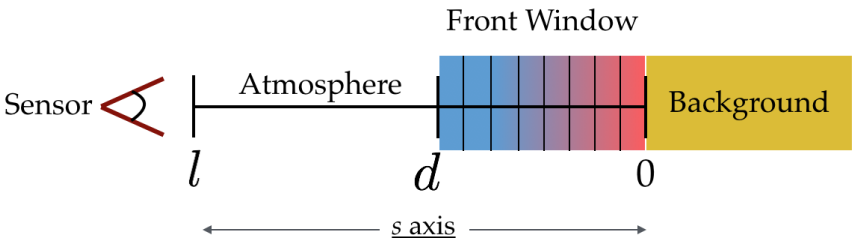

Figure 11. Schematic of the radiative layers used for modeling the radiative effects of the optical viewing window.

it highlights how the total radiance, $L(\tilde{\nu}, s)$ is affected by contributions from different parts of the window in various spectral channels. The total radiance is a combination of L_0 transmitted from behind the window and, depending on the layer of interest, the thermal emission of the window itself from various layers within the glass.

As previously mentioned, the transmissivity for the full thickness of the window has been estimated at two separate temperatures. Using the higher temperature estimated, the weighting function over the total window thickness $W(\tilde{\nu}, 0, d)$ can again be rewritten as:

$$W(\tilde{\nu}, 0, d) = -d^{-1} \ln(\tau_w(\tilde{\nu})) \cdot \tau_w(\tilde{\nu})^{(1-s/d)} \tag{14}$$

where d is the total window thickness and s is some layer between 0 and d. To gain intuition for the relative radiance contributions of different window layers and the spectral dependance of the weighting function, plots of the weighting function over the depth of the window for a highly transmissive and highly opaque spectral band are provided along with the transmission function of the window showing the bands integrated over. These are shown in Figure 12. In the opaque region, radiance contributions from the window surface will dominate. As the window becomes transmissive, however, the weighting function becomes very low but also very uniform indicating that contributions from all window layers will be even.

It is also informative to plot the weighting function over wavenumber for various

www.manaraa.com

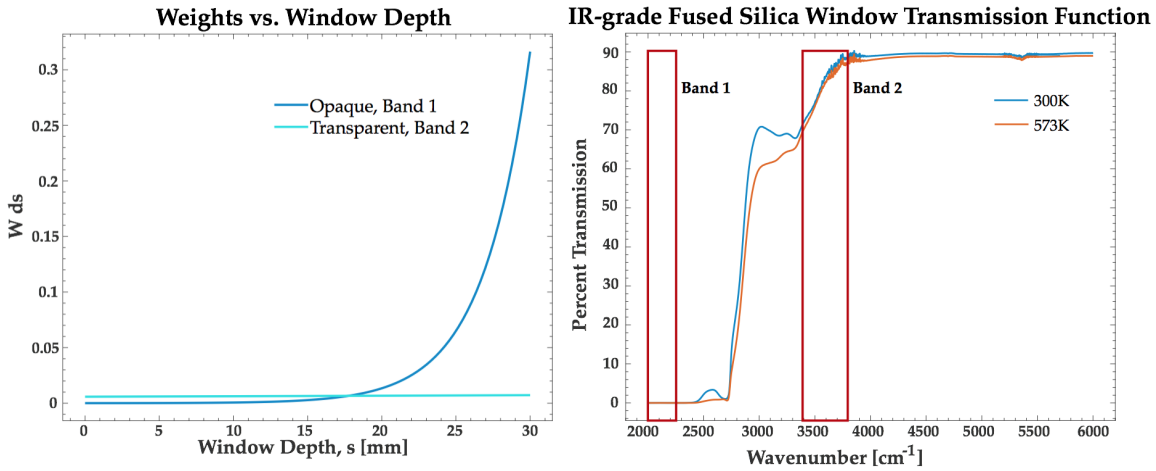

Figure 12. ***Left:*** **Weighting function over window depth for two spectral bands of 2000-2250 cm^{-1} and 3400- 3800 cm^{-1} respectively.** ***Right:*** **Transmission function for the window with the spectral bands of the window marked.**

window depths. Therefore plots of the weighting function for five evenly spaced window layers appear in Figure 13. These are plotted with a log scale for maximum clarity. Again, it is evident that contributions from the surface layer dominates all other contributions. Note first that the shapes of the weighting functions for different layers are all very similar over the measured spectral range, first increasing to a peak, then dropping off to a constant value. Furthermore, the weighting functions for all layers approach the same value starting at 3000 cm^{-1} and by 4000 cm^{-1} have converged to a low value below 0.01%. This behavior is as expected. As the window becomes more transparent, more of the radiance L_0 is transmitted than absorbed, and therefore less radiance can be self-emitted. As we progress to deeper window layers, the spectral location of peak contribution shifts to higher and higher wavenumbers. This is because as the window gradually becomes more transparent, more of the self-emission from back layers of the window are transmitted. Referring back to Figure 13, notice that even at low wavenumber were the window transmission is very low, the contributions from inner layers are non-zero. This is because the transmission function is never truly zero, thus there is no point that the surface layer of the window is the only contributor.

www.manaraa.com

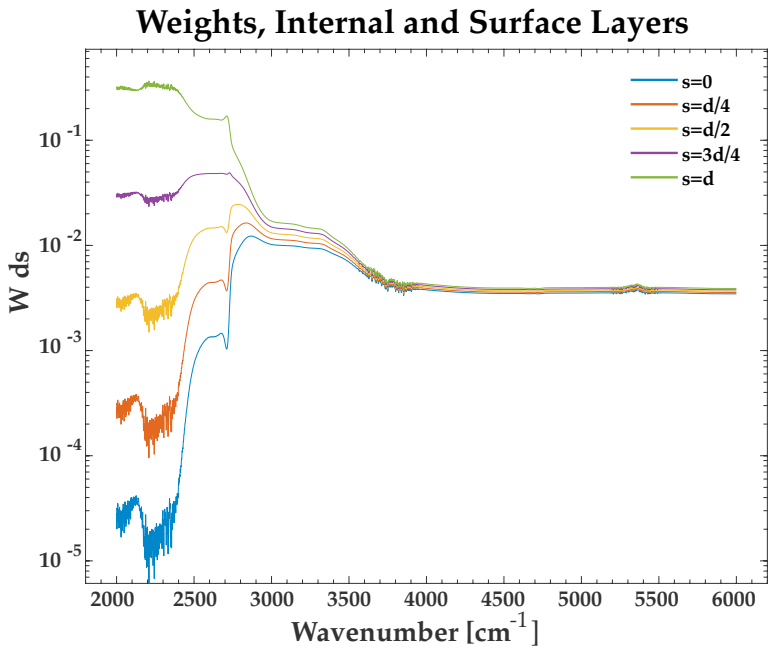

Figure 13. Plots of weighting function over window depth for a transmissive and opaque spectral band

This model provides a basis on which to examine results in spectral bands were window emissions are a significant contributor. One addition model must be developed to allow full insight into the behavior of the window – an estimation of the temperature distribution over the thickness of the window and a method for relating measured radiance to temperature. These are provided in the next section.

2.5 Thermal Estimation Methods

2.5.1 Brightness Temperature Calculations

In the spectral region were the viewing window of the scramjet cavity is almost opaque, the measured radiance can be assumed to originate at the window's surface. The measured radiance in this band can be used to calculate the window's brightness temperature, or the temperature at which a perfect blackbody would produce the same spectral radiance at each wavenumber within the specified band. This calcula-

www.manaraa.com

tion is done using an inverse planckian function, which is shown in Equation 15.

$$T_b(L, \tilde{\nu}) = \frac{hc\tilde{\nu}}{k_B \ln[\frac{2hc^2\tilde{\nu}^3}{L(\tilde{\nu})} + 1]} \tag{15}$$

where a temperature is calculated for each wavenumber's corresponding radiance value. To minimized noise from fluctuations from the data, the mean of the spectral band and measured radiance is taken before performing the calculation, then a single temperature value is assigned to each pixel. If the radiance had been emitted from a perfect blackbody, than the temperature calculated at each wavenumber would have been identical, and no mean would be necessary. However, since the window is only approximated as a blackbody, and the flame behind it exhibits high levels of fluctuation, each pixel has an unique standard deviation in the calculated temperature value. As the window becomes more transmissive, brightness temperature calculations can still be performed. However, the radiance used in the calculations will be contributed from various elements along the line of sight, including the full depth of the window and cavity elements. Thus, while helpful for identifying general trends, it should be noted that the temperatures can no longer be assumed to have a definitive connection to thermal temperature.

Because the brightness temperatures calculated in the region of lowest window transmission have the highest quantitative quality, it is of benefit to explore what kind of information can be gleaned from these calculations.

2.5.2 One Dimensional Thermal Transfer Model

Better understanding of the temperature values measured at the window surface can be gained with knowledge of how heat will travel through the window. To accomplish this, a simple thermal transfer model is used. First consider the one dimensional heat equation

www.manaraa.com

$$\frac{\partial T(x,t)}{\partial t} = a\frac{\partial^2 T(x,t)}{\partial x^2} \tag{16}$$

where a is the thermal diffusivity for the window, $T(s,t)$ is the window temperature at some spatial point x and time t.

A numeric approximation for the solution of the one dimensional heat equation was used to form a model of for the behavior of thermal impulses traveling from the cavity through the window. The numerical approximation used to given in Equation 17

$$\frac{T_i^{(n+1)} - T_i^n}{\Delta t} = a^2\frac{T_{i-1}^n - 2T_i^n + T_{i+1}^n}{\Delta x^2} \tag{17}$$

where the superscripts n represent the time index, the subscripts i represent the space index, and T is the temperature at some point. This model used temperatures from spatial points in the previous time step to find the temperature $T_i^{(n+1)}$ at a spatial point in the subsequent time step. For this model, the initial conditions must be known, and a method for defining the boundary conditions must be established. For the scramjet environment, it was concluded that the most appropriate approximation for the interior boundary condition is a single value, either at the flow field or combustion temperature. The boundary condition for the outer surface of the window was set to abide by the condition

$$\frac{T_{i+1}^n - T_{i-1}^n}{\Delta x} = 0$$

forcing the derivative at the outer surface to be zero.

This model is very simple, and has several limitations. Perhaps the most significant limitation is the lack of any cooling effect. In reality, heat is lost both to adjacent window material in the second and third dimensions as the thermal impulse travels through the window, and to the surrounding air once the surface of the window has

www.manaraa.com

been reached. This model accounts for none of these effects. Furthermore, any heat dependance of the physical parameters are ignored, which given the extreme conditions the material was subjected to during the data collection, the use of physical parameters varying with temperature would be more appropriate. Because of this, the values produced by the model should not be considered indicative of the true temperatures of the modeled environment. However, in spite of these limitations, this model can be used to gain some intuition of the behavior of a thermal impulse traveling through this material. This includes attenuation of the thermal impulse by the window in one dimension, the time scales for transfer of thermal impulses, and the time required for the window to reach thermal equilibrium.

To illustrate the use of the model, the Figure 14 shows the temperature profiles produced by the model for two different temperature impulses applied to the window for 30 seconds from thermal equilibrium. The plots below these show 30 seconds of cooling when the internal window temperature returns to the equilibrium temperature of 450°K. Profiles are plotted every three seconds with the lighter colors plotted later in time. The impulse temperatures where chosen from the approximate range of combustion temperatures that will be encountered in the subsequent data. The equilibrium temperature is chosen from the approximate temperature of non-combusting flow field. From these results, it is clear that the shape of the temperature profile will vary little with the temperature impulse. If we consider the temperature at the window surface, however the change in temperature for the high and low temperature impulse is revealing. The change in temperature between the first and last profile at the window surface are tabulated below in Table 1. Over the course of the burn, the temperature increase at the surface of the window is not significantly different for the high and low temperature impulses. However, when the interior boundary of the window is returned to the previous equilibrium temperature and the impulse is

www.manaraa.com

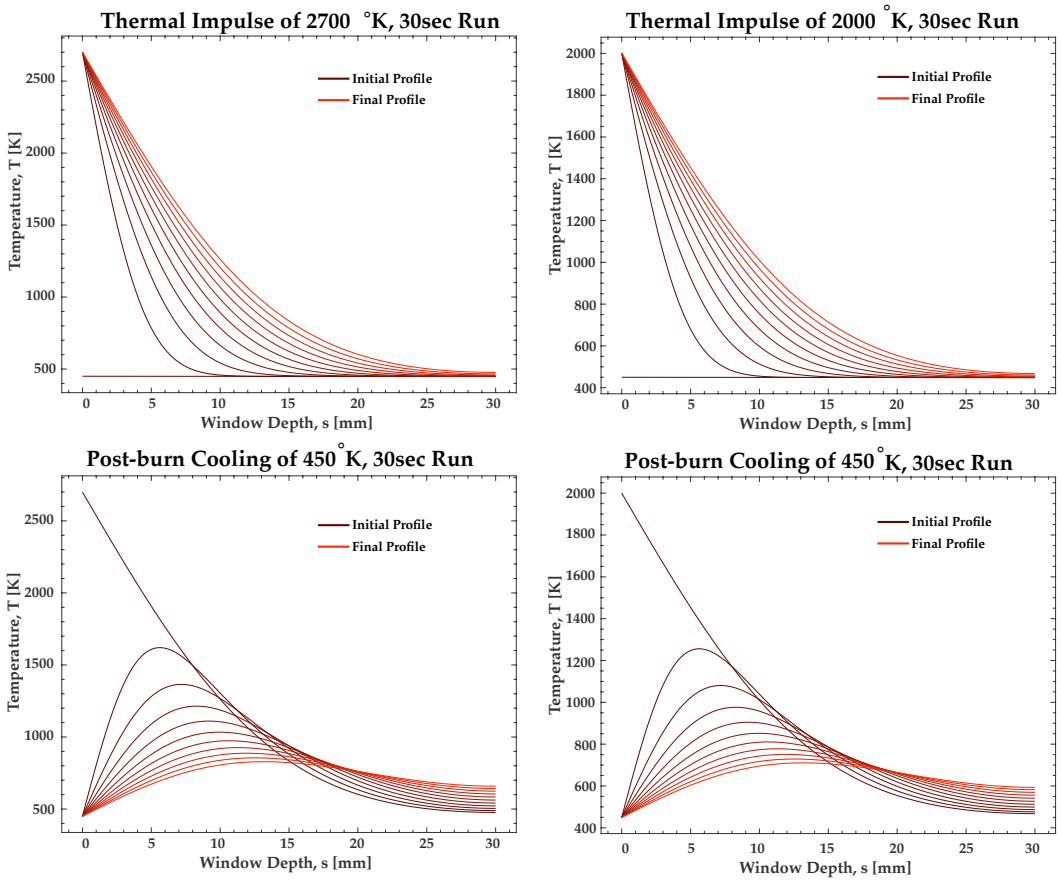

Figure 14. Illustration of temperature profiles for 2700°K and 2000°K thermal impulses. Profiles shown before, during and after each burn. A profile is drawn for every three seconds the model is run.

allowed to travel through the window for an additional 30 seconds, the temperature increase at the window surface is significantly higher for the high temperature impulse than the low temperature impulse. Therefore, for the material composing the viewing window for these experiments, a time delay of 45 to 60 seconds from the beginning of combustion is expected before significant heating on the surface of the window is observed.

One additional trend worth exploring with our model is how consecutive thermal impulses effect the evolution of the window's temperature profile. To test this effect, a thermal impulse of 2700°K was applied to the window for 30 seconds, then the

www.manaraa.com

Table 1. Predicted Temperature Change at Outer Window Surface

	2700 K Burn	2000 K Burn	2700 K Post-burn	2000 K Post-burn
Δ T [K]	17.8	17.5	182.3	125.7

internal temperature of the window was returned to the equilibrium temperature of 450°K for 30 seconds, then the high temperature was applied again for another 30 seconds. This process was repeated 3 times, and the profiles at the end of each 30 second burn and cooling period were plotted. These plots are shown in Figure 15 Note that the increase in temperature at the window surface between Impulse 1 and

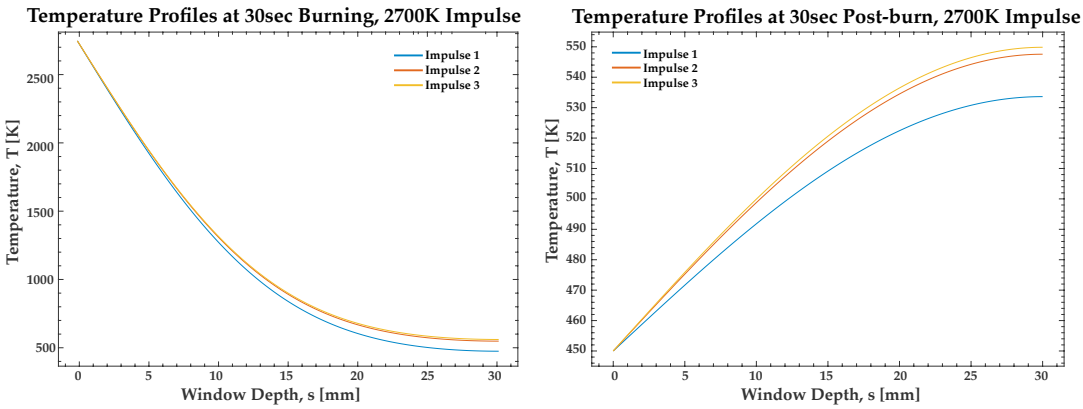

Figure 15. ***Left:*** **Final temperature profiles after 30 seconds of burning for three consecutive 2700 K thermal impulses.** ***Right:*** **Final temperature profiles after 30 seconds of cooling for the thermal impulses shown on the left.**

Impulse 2 is significantly greater than the increase between Impulse 2 and Impulse 3 for both the burning and cooling profiles. The difference in temperature at the window surface between each of these impulses is provided in Table 2.

Table 2. Predicted Difference in Window Surface Temperature for Successive Impulses

	Burn, 1 to 2	Burn, 2 to 3	Cooling, 1 to 2	Cooling, 2 to 3
Δ T [K]	72.2	11.8	13.9	2.3

www.manaraa.com

From these figures and values, it is evident that for repeated impulses, the window experiences a kind of thermal saturation effect and the effect at the window surface is mitigated.

www.manaraa.com

III. Experimental Setup and Data Collection

3.1 Setup and Instrument Settings

AFIT and AFRL collaborated in an experimental effort imaging reacting C_2H_4 fuel plumes in a scramjet cavity over three days of testing. The objective of these tests was to gain spatially resolved estimations of the temperature and species concentrations[3]. The experimental setup for this test is outlined in Figure 16 and described below. This effort included data reduction, calibration, an initial assessment of the data's quality, and early analysis of values such as scalar concentrations and distributions[3].

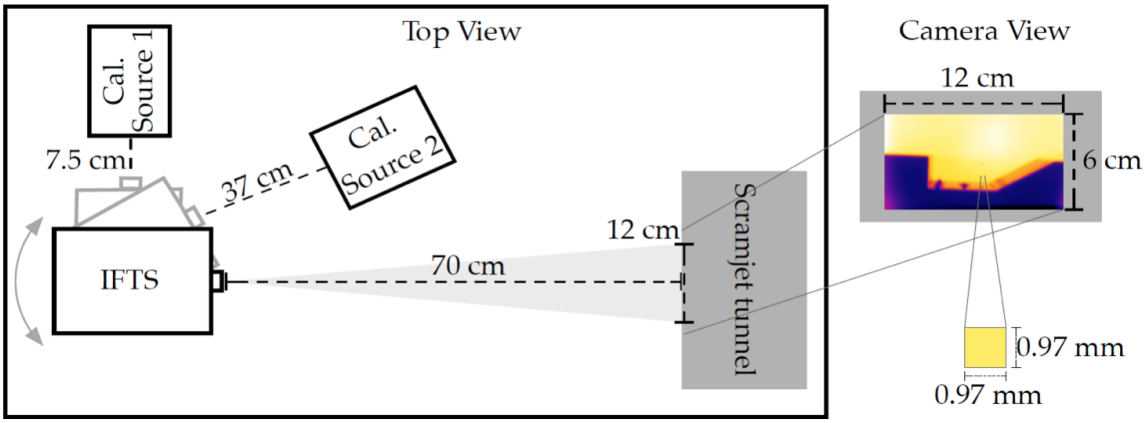

Figure 16. Setup for hyperspectral imaging of a scramjet cavity

The Telops Hyper-Cam hyperspectral camera (mid-wave IR: 1.5−5.5 μm) was used to capture the hyperspectral data sets. Againg, the reader is referred to the literature for exhaustive descriptions of the instrument[25, 4], as only a brief description is provided here. The Telops has a removable 0.25 × telescope, which was used for this experiment. With the telescope, the camera has a 0.47 rad × 0.38 rad field-of-view (FOV) over the 320×256 focal-plane array (FPA), corresponding to 0.5 × 0.5 mm^2 per pixel at the minimum working distance of 33 cm. Imaging window size

www.manaraa.com

is fully adjustable from 320×256 pixels to 64×64 pixels. Spectral resolution is fully adjustable from $150\,\mathrm{cm}^{-1}$ (coarse) to $0.25\,\mathrm{cm}^{-1}$ (fine). For these tests, the camera was set 70cm away from the window of the test rig. The FPA was set to 128×64 pixel sub-window, and the spatial resolution of one pixel was a 0.97mm $\times$ 0.97mm area at the image plane. The optical center for this configuration was located approximately 2cm above the cavity floor. The image capture integration time was set to 20μs. The spectral resolution was $4\mathrm{cm}^{-1}$, which corresponds to an interferogram maximum OPD of 0.15cm.

Data for the spectral calibration was taken of a 15.25 cm square EOI blackbody and a 2.54 cm cavity CI systems blackbody. These sources were respectively placed 37 cm and 7.5 cm away from the front optic of the camera, in an attempt to ensure the entire FOV of the camera viewed the blackbody source. Spectral emissivities for the 2.54 cm and 15.25 cm blackbodies are reported to be 0.96±0.02 and 0.99±0.01, respectively. The test platform for these series of tests was a continuous supersonic

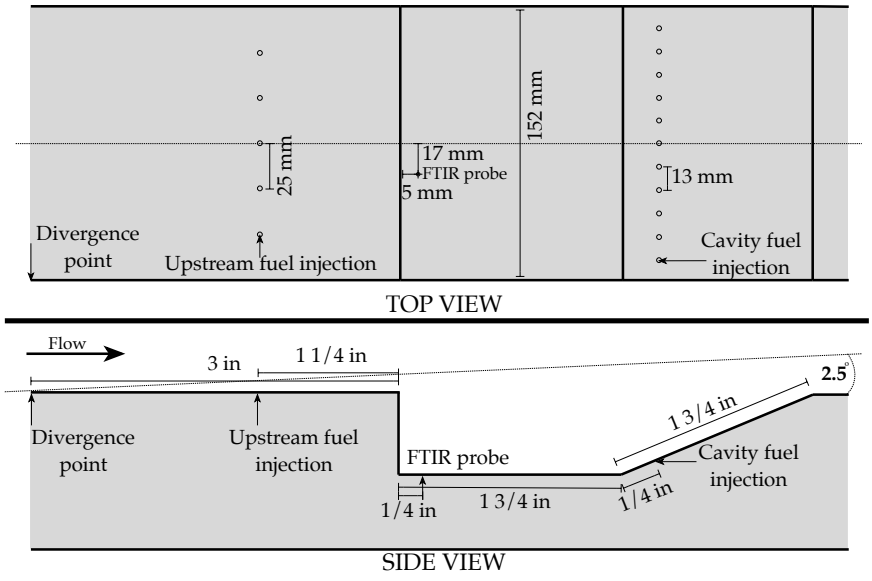

Figure 17. Schematic of the scramjet cavity.

www.manaraa.com

wind tunnel with a model combustor, located in AFRL's Research Cell 19 on WPAFB. The tunnel operated at approximately Mach 2.2 with a total temperature of 590K. Gaseous methane (C_2H_4) injection into the cavity ranged from 50 to 110 slpm. Fuel was injected at the base of the cavity on the ramp and ignited for 30 second periods. A schematic of the cavity is shown in Figure 17. Radiance from the combustion was viewed through a 3cm thick Corning 7979 IR-grade fused silica window. This material comprised both of the side walls within the cavity.

3.2 Data Collection

Data was collected on November 14th, and a subset of this data is analyzed. On the evening of the 14th, hot vitiated air was pumped through the system, producing a flow field traveling at approximately Mach 2.2. This hot air ran through the system for several minutes allowing the system to reach thermal equilibrium. After the thermal equilibrium was reached, a test burn using fueling conditions of 75 sLpm and cavity only fuel input was run. This was done to ensure the test cell environment was appropriate for additional tests. Four fueling rates were then run several times over the course of the evening. The four fueling conditions run repeatedly were 50, 70, 90, and 110 sLpm using cavity only fuel input. Table 3 provides these fueling rates with their approximate local fuel to air ratio, and peak combustion temperatures as reported by the NASA's Chemical Equilibrium with Applications (CEA) program. Within this work, the first and second sets of these fueling conditions will be analyzed. The first set includes the test run, which provides the initial heat impulse to the window, increasing its temperature from equilibrium. The first fueling run of each of these sets are taken approximately 45 minutes apart. It should be noted that the order in which the fueling rates are run varied, as there were times the thermal conditions were not appropriate for the ignition of the fuel lean case of 50 sLpm, or

www.manaraa.com

Table 3. Fueling Conditions, Parameters

Fueling Rate	Fuel to Air Ratio	CEA Temperature [K]
50 sLpm	0.81	2425
70 sLpm	1.1	2696
90 sLpm	1.37	2504
110 sLpm	1.63	2337

the fuel rich case of 110 sLpm. When non-ignition occurred, the more optimal cases of 70 or 90 sLpm were run, and the other cases were run at a subsequent point in the sequence.

www.manaraa.com

IV. Results

The greatest strength of the IFTS as a diagnostic instrument is the variety of information captured in a single data cube. Several different methods of analysis and representation are used to produce the final results, thus the first section presents a brief summary of the different kinds of data representation and their interrelations. Following this, the results are considered in detail, and provide insight into window spectral contributions over the midwave IR, window temperature and evolution over time, and noise bias.

4.1 Data Representations

The IFTS captures data in 4 dimensions: x and y spatial dimensions, a spectral dimension, and time. All data representations are created by either taking a discrete point, or averaging over some dimension. For example, and image of the cavity's radiance can be displayed by taking a spectral average for one or many time steps. A full spectral can be displayed by looking at a single pixel for a single time step, or by taking a spatial or time average. Since the radiance contributions of the window are spectrally dependent, displaying images that average smaller bands of the camera's full bandpass lead to insights of the radiance contributions of different elements along the line of sight. Figure 18 shows how images averaged over different spectral bands provide unique emission profiles.

The data in the above figure is taken at a single sample point in time. The top figure shows a plot of a spectra averaged over a small spatial region of pixels viewing the cavity combustion. The transmission function of the window for 573°K is also plotted. The three images below show the cavity radiance in different spectral bands. The first images shows a band where the window transmission is effectively

www.manaraa.com

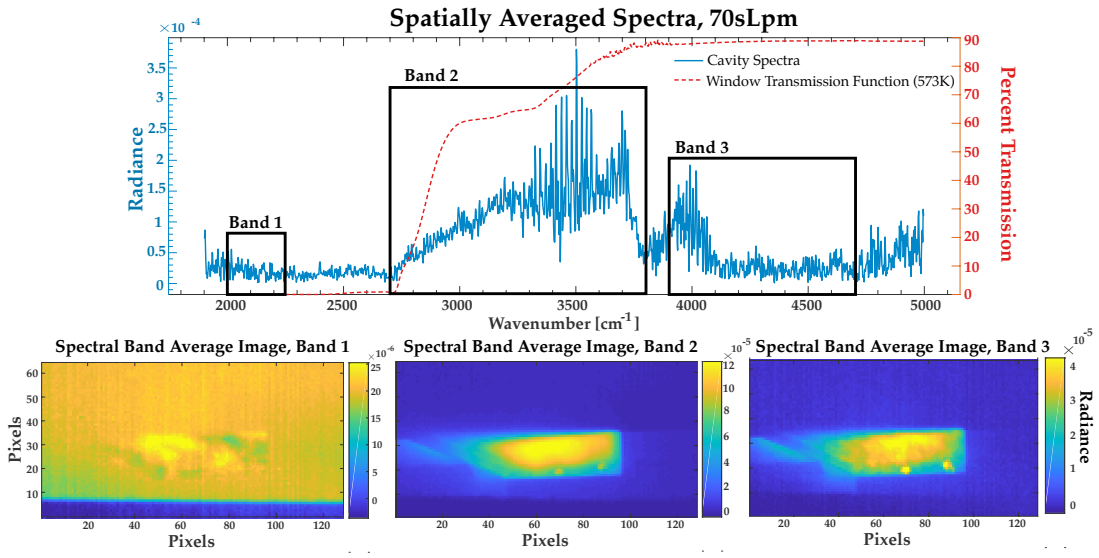

Figure 18. Spectrally integrated images for different spectral bands

zero, while the second and third images respectively show bands where the window transparency increases from zero to 90 percent, and where it is stable at 90 percent. The appearance of combustion effects in the opaque region of the is a phenomena that will be examined in the results section. Each of these images show different behavior for the cavity's emission.

Examination of the emission trends over time can also be accomplished by taking a spatial average in some spectral band for each time sample point. If we average over the spectral band where the window is effectively opaque and convert radiance to brightness temperature using methods previously described, the surface temperature of the window over time can be examined.

All of the following results are given using one of these representations. Often the same trends will be explored through several different representations. Justification for the selection of particular regions averaged over, or the discrete points chosen will be provided before each result.

www.manaraa.com

4.2 Window Surface Brightness Temperature

4.2.1 Data Set 1

The first results we will consider are of the outer surface temperature of the window for representative runs from Data Set 1 and 2. The spectral band chosen to examine the opaque region of the window was 2000-2250 cm^{-1}. Figure 19 shows the transmission function of the window, and the spectral region which was averaged to create the radiance maps. This spectral band is between the camera's lower bandpass cutoff and a significant atmospheric CO_2 absorption feature centered between 2300-2400 cm^{-1}. Thus the emission from the 2000-2250 cm^{-1} can be assumed to be predominately from the window surface, and experiences minimal attenuation while propagating to the detector. First, consider a radiance map of the outer window before any combustion has occurred. This is shown on the left in Figure 20. There is hot vitiated air flowing through the tunnel, and there has been ample time for the window to reach equilibrium. There is greater radiance emission at the top of the baseline radiance image shown in Figure 20 where the vitiated air has been in continual contact with the window. The bottom area of the window has less emission as it is in contact with the metal components of the cavity and is therefore has some insulation from the hot air. Note that the radiance range is very small, so the insulating effect is minimal. Since the emission is dependably from the outermost layer of the window and the atmospheric attenuation is minimal,

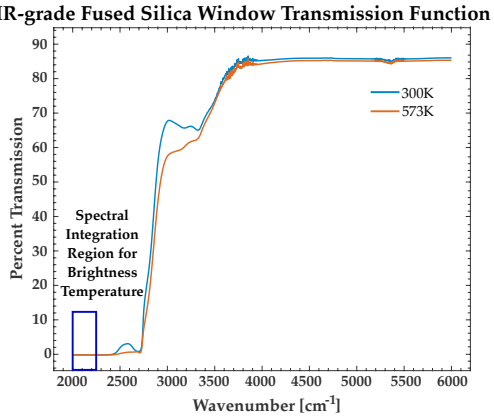

Figure 19. Window transmission function showing the spectral band integrated over to examine the outer surface of the window.

www.manaraa.com

the radiance in this spectral band can be converted to brightness temperature using the method detailed in the background section and be assumed to provide a good approximation of true temperature. Performing this conversion on the pre-combustion window emission, we get the result shown on the right in Figure 20.

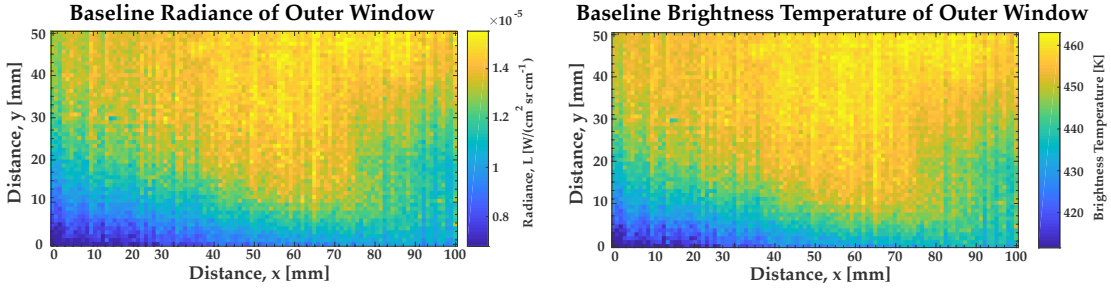

Figure 20. ***Left:*** **Pre-combustion baseline radiance emission from window surface.** ***Right:*** **Baseline radiance converted to brightness temperature for window surface.**

Again, the upper area of the window is slightly warmer than the lower area due to being in direct contact with the hot flow field, resulting in a variation from highest to lowest temperature of approximately 50°K. At the time of this data collection, the hot air had been flowing for approximately 20min. Based on the results of our simple thermal transfer model shown in the background section, there has been sufficient time for the window to reach thermal equilibrium with the flow field. Thus, by taking the average of the brightness temperature over the displayed spatial region, we can say that the approximate starting temperature of the entire thickness of the window is 447°K. From this, we can then examine the progression of the outer window temperature by calculating the brightness temperature prior, during, and post combustion for consecutive fueling runs.

Since the amount of data recorded before and after combustion varies with each run, comparison of the prior, during, and post combustion window surface temperatures

www.manaraa.com

is best accomplished by taking a single data cube at some time before and after combustion. The data cube showing the burn is then selected some fixed number of time steps after the pre-burn data cube. Thus, comparison of the prior, during, and post combustion is accomplished by taking discrete time points, and averaging over a spectral band. Figure 21 displays images of the prior, during, and post combustion brightness temperatures for each of the fueling runs in the Set 1 data.

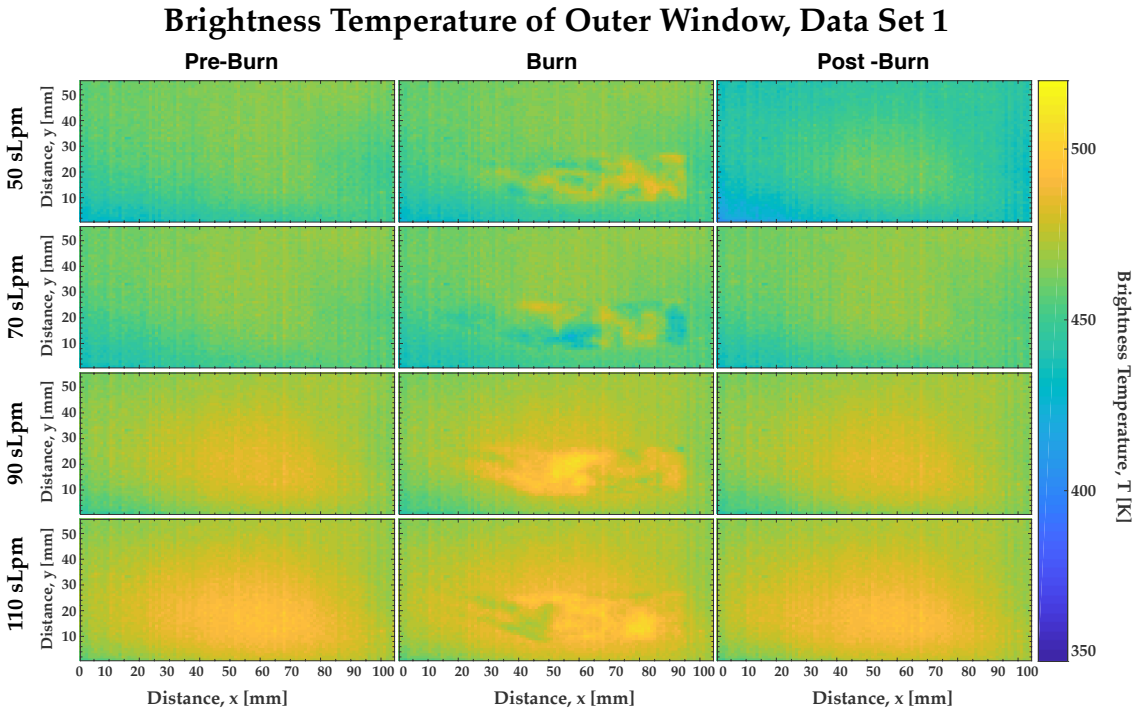

Figure 21. Brightness temperature maps of particular times prior, during, and post combustion for consecutive fueling runs.

Figure 21 allows for the comparison of the increase in temperature over successive runs, and the difference in temperature between 1 second before ignition, $\tilde{1}5$ seconds into the 30 second burn, and 0.5 seconds after combustion has ended. The images shown during the burn exibites notably warmer regions where the combustion is occurring. This high temperature bias in the cavity region is caused by significant

www.manaraa.com

noise effects. This effect will be further explored and analyzed in the next section, and will merely be observed in this section. Focusing attention on the pre and post burn images, it is clear that the window's temperature increases over successive fueling runs. However, temperature differences between the window's pre and post burn images is not evident. Further exploration of these trends is done by calculating the spatially averaged temperature and standard deviation for each fueling rate's pre and post burn images. These numbers are reported in Table 4. From the average

Table 4. Average Temperatures for Pre and Postburn Frames, Data Set 1

Fueling Rate	Preburn Temperature [K]	Postburn Temperature [K]
50 sLpm	456.8 ± 1.67	445.1 ± 1.91
70 sLpm	459.6 ± 1.57	460.0 ± 1.59
90 sLpm	471.3 ± 1.49	470.9 ± 1.51
110 sLpm	478.0 ± 1.51	477.4 ± 1.51

temperatures, we see that the temperature remains constant between the pre and post burn images for all fueling runs with the exception of the 50 sLpm fueling run. Also, note that for all runs temperature has increased by the time the pre burn image for the subsequent fueling run is taken. For the 50 sLpm run, the average window surface temperature has dropped by 10°K. These trends initially seem strange, however when we consider that the thermal impulsed from the combustion takes time to travel through the total window thickness, it is reasonable to assume that from the start to the end of the burn, the outer window is showing the cooling effects that would have taken place between the end of the previous burn, and the start of the current burn. It is then in the time following the combustion end that the hot thermal impulse has sufficient time to travel from the inner to outer layer of the window. Thus, we would expect that the average temperature of images taken at greater

www.manaraa.com

times post combustion would be greater, leading to the higher temperatures taken prior to combustion for successive runs. This theory can be tested by looking at the frames from two different frames taken after the burn – one at 1 second post-burn which was previously displayed, and and the last post-burn frame taken after each burn. These results are shown in Figure 22

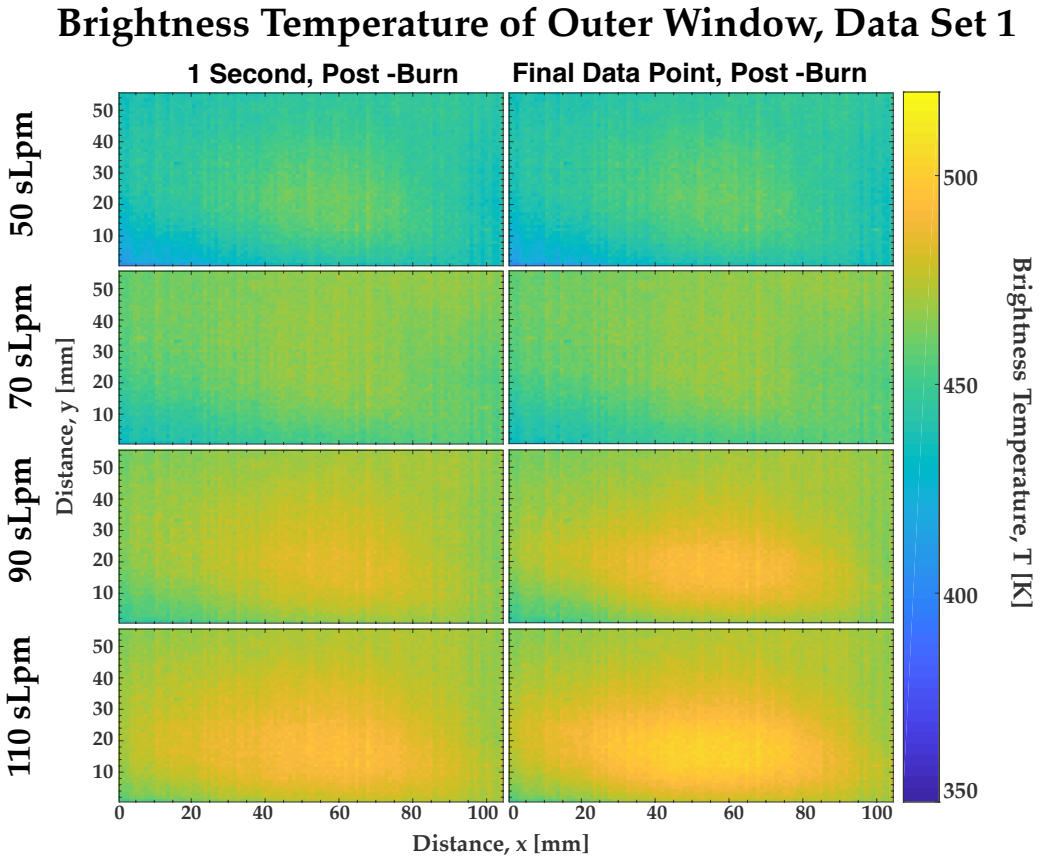

Figure 22. Brightness temperature maps of frames taken 1 second post-burn and at the end of the data collection.

Here, heating trends between the two displayed frames are evident in the 90 sLpm and 110 sLpm cases, but still obscure in the case of the 70 sLpm and 50 sLpm rates. Again tabulating the average temperatures of each frame, along with the length of

www.manaraa.com

time post-burn the final frame was collected, Table 5 contains the results. Using this

Table 5. Average Temperatures for Postburn Frames

Fueling Rate	1st Frame Temp [K]	Final Frame Temp [K]	Frame Delta t
50 sLpm	445.1 ± 1.91	445.2 ± 1.91	15.0
70 sLpm	460.0 ± 1.59	459.9 ± 1.60	2.9
90 sLpm	470.9 ± 1.51	473.7 ± 1.60	18.4
110 sLpm	477.4 ± 1.51	480.5 ± 1.70	16.5

results, a the lack of temperature increase in the 70 sLpm is likely caused by the short length of time over which post-burn data was collected. The surface of the window has still not had time to heat. The lack of temperature increase in the 50 sLpm is still without obvious explanation, but will be addressed further in the following analysis.

The post-burn heating trends can be more fully observed by taking a spatial average for a sub-region of pixels, and plot this averaged temperature for successive time steps. This method of data visualization can also be used to see the amount of time between the runs, and therefore, the amount of time cooling is taking place before the next thermal impulse. To orient the reader to the next series of results that will be displayed, Figure 23 shows the spatial region averaged over to create a single temperature value, and the resulting temperature points for all the runs on an absolute time scale, taking the test run as time zero. The average spatial region was chosen because it covers only the combustion cavity. Thus, the primary radiance contributions to window heating will have come directly from the combustion event, rather than from adjacent window heating or hot metal elements. While Figure **??** does not clearly show the heating trends before, during, and after the burn, we can see the time between the fueling runs of interest, and note the comparative time that cooling was allowed to take place. These separation times are important to

www.manaraa.com

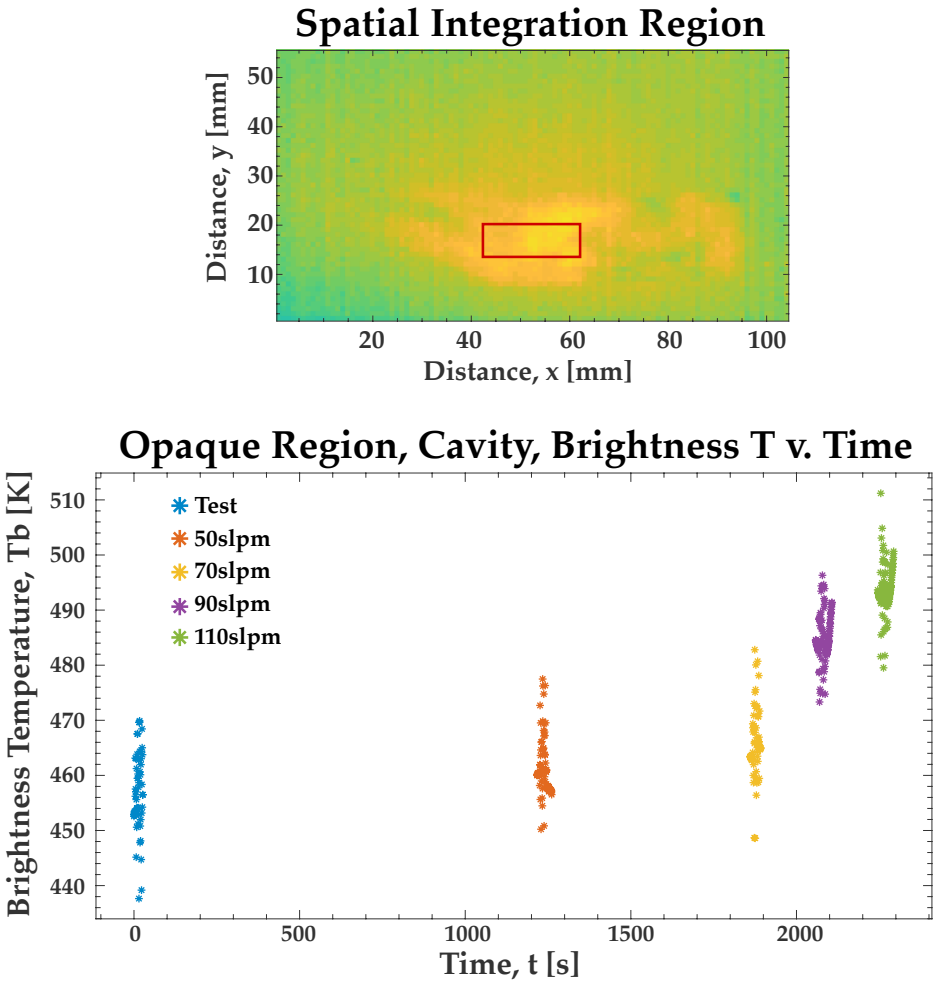

Figure 23. ***Top:*** **Temperature map showing the region averaged over to produce the temperature vs. time plots.** ***Bottom:*** **Temperature vs. time for all the fueling runs on an absolute time scale**

highlight, as the cooling time will significantly alter the heat propagation profile for the consecutive run, and the cooling times displayed are not uniform.

Having now established context, Figure 24 displays temperature over time for all the data runs on a broken time axis. The first notable feature of this plot is the sharp increase in temperature bias and noise that occurs within each run. Again, these are noise effects from the combustion and will be explored in the next section. If we removed these burn effects and focus on the data before and after the burn, the trends depicted in Figure 25 become evident. The 90 sLpm and 110 sLpm fueling

www.manaraa.com

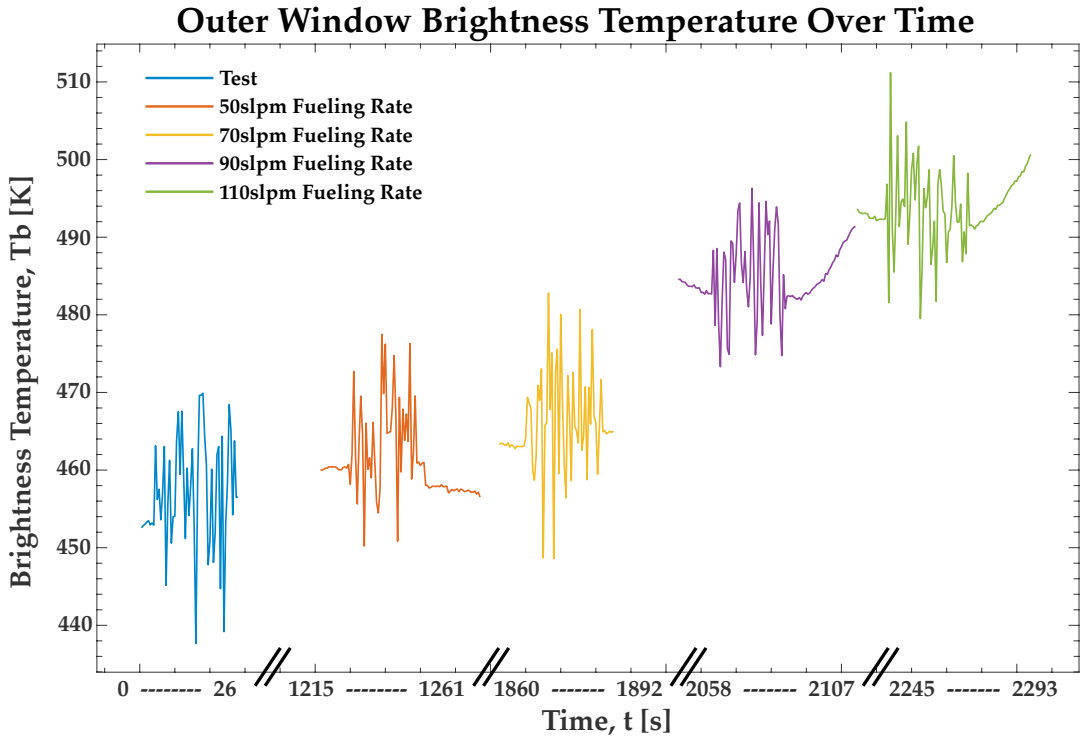

Figure 24. Temperature vs. time for all fueling runs, broken time axis

conditions had the greatest pre and post combustion data collection, so these trends will be examined first. For these two fueling runs, note first that the pre-combustion temperature exhibits a clear downward trend for both cases due to cooling. The temperatures measured at the beginning of the post-combustion data indicate that on the outer window, the cooling continued through the burn. Shortly after the end of the combustion, the temperature exhibits an increasing trend that continues to the end of the data collection. This increase has very linear behavior, and shows no sign of leveling off by the end of the data collection.

Now considering the other three fueling conditions: the Test has too little data on pre or post combustion to see distinctive trends, however we do see an initial temperature at approximately 455°K and final temperature of approximately 458°K. Note that starting temperature here is biased higher than the one previously calculated.

www.manaraa.com

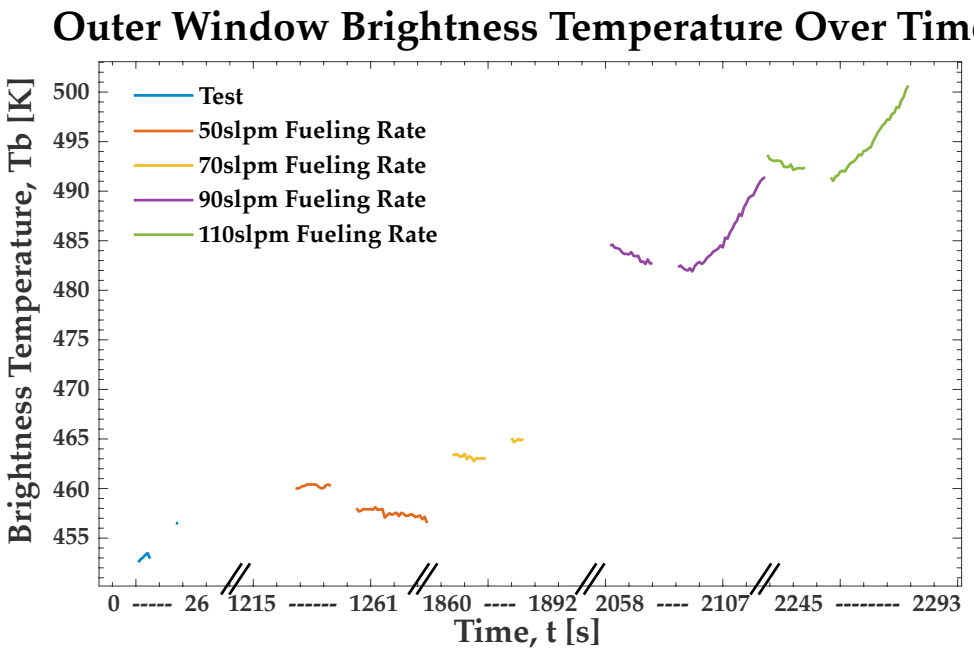

Figure 25. Temperature vs. time for all fueling runs, broken time axis

This is because the previous average included all of the pixels measuring the window, while this average is taken with a subset of the previous pixels. Also note that immediately after the burn, the temperature appears to have risen. There is not sufficient data taken after the test burn to determine if this trend it persists, but it is what we would expect to see since the window surface started at it's coolest temperature and therefore begin heating shortly after the thermal impulse. Both the 50 sLpm and 70 sLpm fueling rates exhibit somewhat unexpected behavior. Prior to combustion, both surface temperature plots appear relatively stable, though the 70 sLpm pre-combustion temperature is higher than that of the 50 sLpm. After combustion, the temperature after 50 sLpm has dropped by approximately 5°K, and appears to continue to hold this temperature over time, if not dropping slightly. The post 70 sLpm combustion, in contrast, has risen notably from pre to post combustion, though there is not sufficient data taken after combustion to determine the temperature trend over time.

www.manaraa.com

It may be possible to explain the window surface temperature trends after the 50 sLpm and 70 sLpm combustion by considering the amount of heat release each rate produces. Since the 70 sLpm rate produces fuel distributions much closer to the ideal stoichiometric values, it is reasonable to expect that more of the fuel would burn, leading to greater heat release. The 50 sLpm is a fuel lean rate, and having less fuel to burn may have less energy release – possibly a smaller quantity than any other fueling rate. During the experiment, the 50 sLpm often had to be run shortly after a more stoichiometric rate, as the cavity was often too cold for ignition of the 50 sLpm. Thus, the thermal impulse caused by the 50 sLpm rate may not be sufficient to heat the outer window over the time scales we are observing, thus cooling effects are measured instead. Also note that since the 50 sLpm was the first thermal impulse delivered to the window, more of the heat would have been dissipated to the 2nd dimension across the volume of the window, which would slow the heating effects. In contrast, the 70 sLpm rate possibly delivers such a strong thermal impulse to the window that the outer window experiences heating over a comparatively short time, though it is difficult to say if the increase in temperature observed immediately after the 70 sLpm burn is from the 70 sLpm impulse, or the 50 sLpm finally traveling to the window surface. The stability of the temperature prior to these fueling rates can be explained by referencing back to Figure 23 and observing the elapsed time between the Test, 50 sLpm, and 70 sLpm fueling rates. Between these three rates, the elapsed time is on the order of several minutes, thus it is expected that the outer window temperature would be approaching equilibrium. Therefore, over these timescales the temperature would appear stable. This is in contrast to the time between the 70 sLpm, 90 sLpm, and 110 sLpm fueling rates, which are on the order of 2-5 minutes. After these burns, a sharp decrease in temperature would be expected. These are the trends observed in the simple model in the Section II.

www.manaraa.com

The contemplation of the amount of heat released by each fueling rate leads to the question of if this can be quantified in some way by considering the changes in the window surfaces brightness temperature. The first step in this analysis would be to take the lowest temperature either before or after the thermal impulse created by fuel combustion, and compare it to the highest window temperature measured after the impulse. Since the window's temperature increases with each successive fueling run, only the change in temperature can be compared between fueling rates. The points taken to represent the lowest and highest recorded brightness temperature are shown in Figure 26.

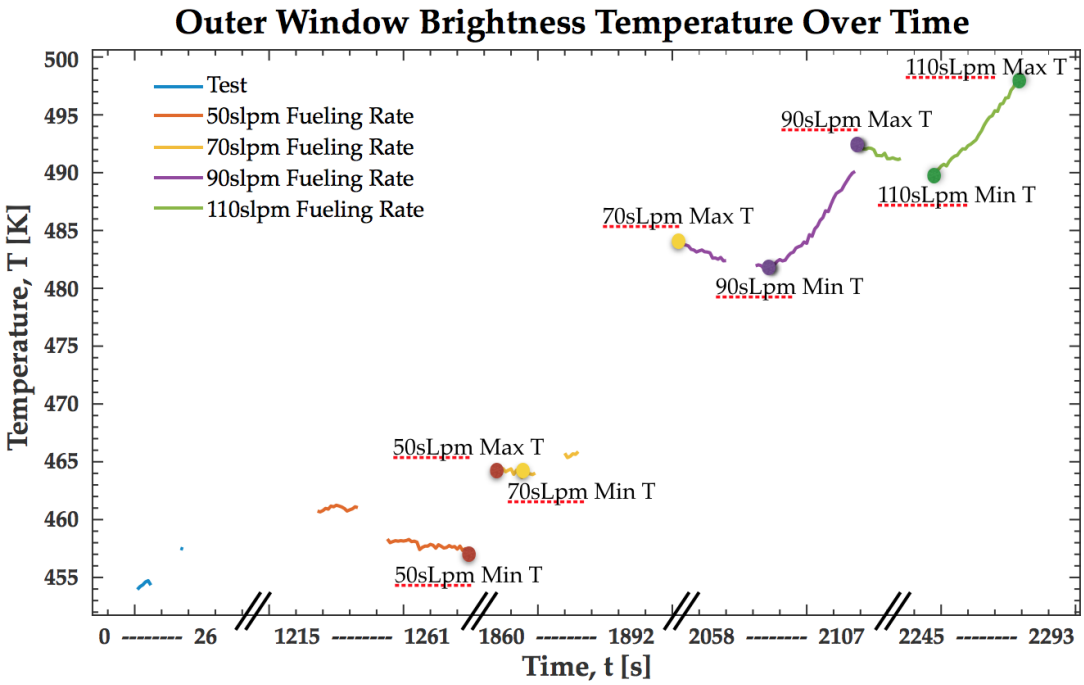

Figure 26. Maximum and minimum temperatures associated with fueling condition

Note that the maximum temperature associated with a fueling rate is consistently taken to be the peak temperature recorded shortly before the next burn. This is because any temperature recorded after one burn and before the next burn can be

www.manaraa.com

assumed to be caused by the thermal impulse of the prior burn. The values for these minimum and maximum measured brightness temperatures, as well as the difference between these temperatures are recorded in Table 6. It should be noted that these

Table 6. Minimum and Maximum Window Surface Temperatures for Each Fueling Rate

Fueling Rate	Minimum Temperature [K]	Maximum Temperature [K]	Delta T
50 sLpm	456.5	463.3	6.8
70 sLpm	462.8	484.6	21.8
90 sLpm	482.0	493.7	11.7
110 sLpm	491.0	500.7	9.7

estimates for ΔT's are limited by the time we were recording data. The full heating and cooling process between the burns was not recorded, thus any calculations done using these ΔT will be rough estimates at best. However, the exercise appropriately illustrates an additional information that can be mined from the data.

It is evident from the above analysis that longer recording times pre and post burn would enable further insight into window surface heating trends. Fortunately, the second set of repeated fueling conditions contain greater amounts of pre and post burn data. The next section will repeat the above analysis for this data set, and conclusions about trends – informed by both data sets – will be reported.

4.2.2 Data Set 2

The last burn of Data Set 1 and the first burn of Data Set 2 were started approximately 30 minutes apart from each other. It should not be assumed that the window was able to return to thermal equilibrium in this time. Before Data Set 1, the window came to equilibrium by being gradually heated via vitiated air, whereas prior to Data Set 2 the window is returning to equilibrium via cooling after being

www.manaraa.com

heated by several sharp thermal impulses. There is no reason to assumed that the time required to return to equilibrium should be similar for these two conditions.

As with Data Set 1, we will begin analysis by examining the window surface brightness temperature at discrete times prior, during, and after the burn. These are shown in Figure 27. As in Data Set 1, this images are taken approximately 1

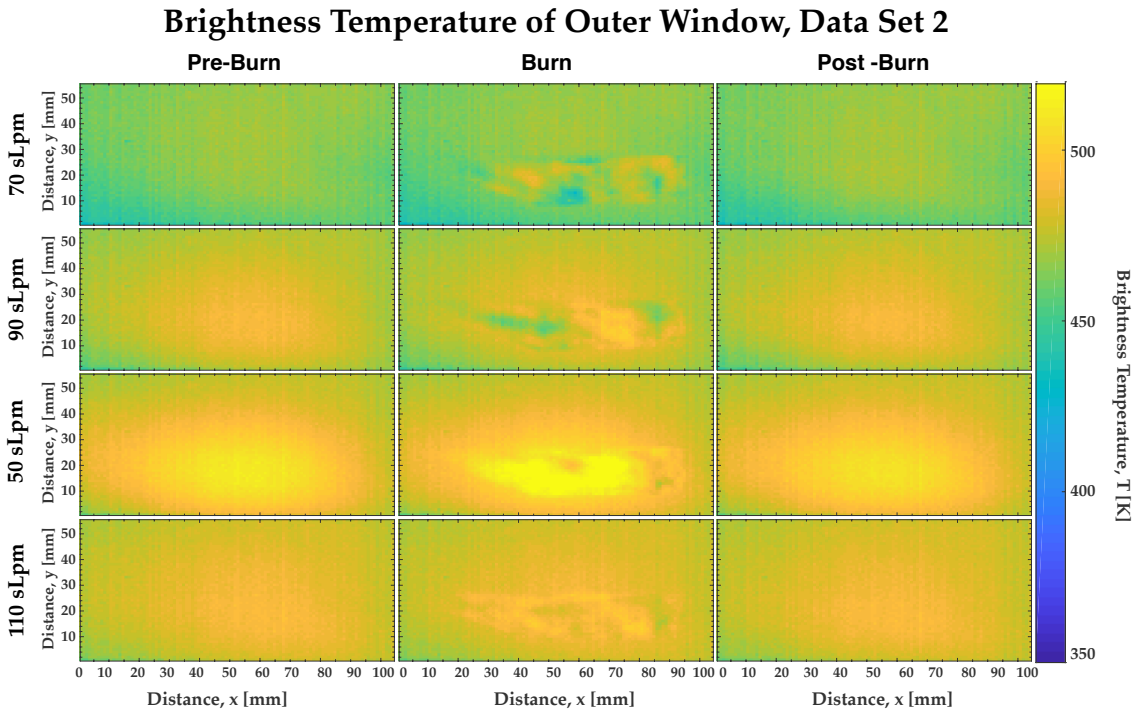

Figure 27. Brightness temperature of window outer surface prior to, during, and after combustion

second before ignition, 15 seconds into the 30 second burn, and 0.5 seconds after combustion has ended. Note first that the order in which the four fueling rates were run is different than for Set 1, with the 50 sLpm run third in the sequence instead of first.

Possibly the most interesting trend here is that the window surface temperature is highest before and after the 50 sLpm burn and has distinctly cooled by the time

www.manaraa.com

the data for the subsequent 110 sLpm fueling rate is recorded. This is consistent with the theory proposed in the previous section that the energy release for the 50 sLpm rate is significantly lower than for the other fueling rates. This theory will continue to be explored throughout this section. Again, the pre and post burn temperatures seem to be very similar. Calculating the average temperature for the pre and post burn images yields the values reported in Table 7. The variation in temperature

Table 7. Average Temperatures for Pre and Postburn Frames, Data Set 2

Fueling Rate	Preburn Temperature [K]	Postburn Temperature [K]
70 sLpm	462.5 ± 1.39	463.5 ± 1.40
90 sLpm	476.9 ± 1.36	476.8 ± 1.36
50 sLpm	488.4 ± 1.64	487.5 ± 1.53
110 sLpm	481.2 ± 1.22	481.0 ± 1.24

immediately before and after the burn is minimal, with the greatest variation being an increase of 1°K for the 70 sLpm. This indicates that the timescales for thermal transfer are comparable to those seen in Data Set 1, though the temperatures are higher for the Data Set 2. Also, noting the pre-burn temperature calculated for the 70 sLpm fueling rate, it is approximately 16°K above the previously calculated equilibrium temperature of 447°K. A plot of temperature over time is now generated for this data set using the same method previously described, and is shown in Figure 28.

These runs were taken in much quicker succession than in Data Set 1, therefore a broken time axis is not necessary to clearly display all of the data simultaneously. From Figure 28, it is evident there was a higher level of consistency in the amount of data taken before and after the burns, therefore the trends in the temperature are more apparent. For the 70 sLpm burn, which was completed first in this data set, we

www.manaraa.com

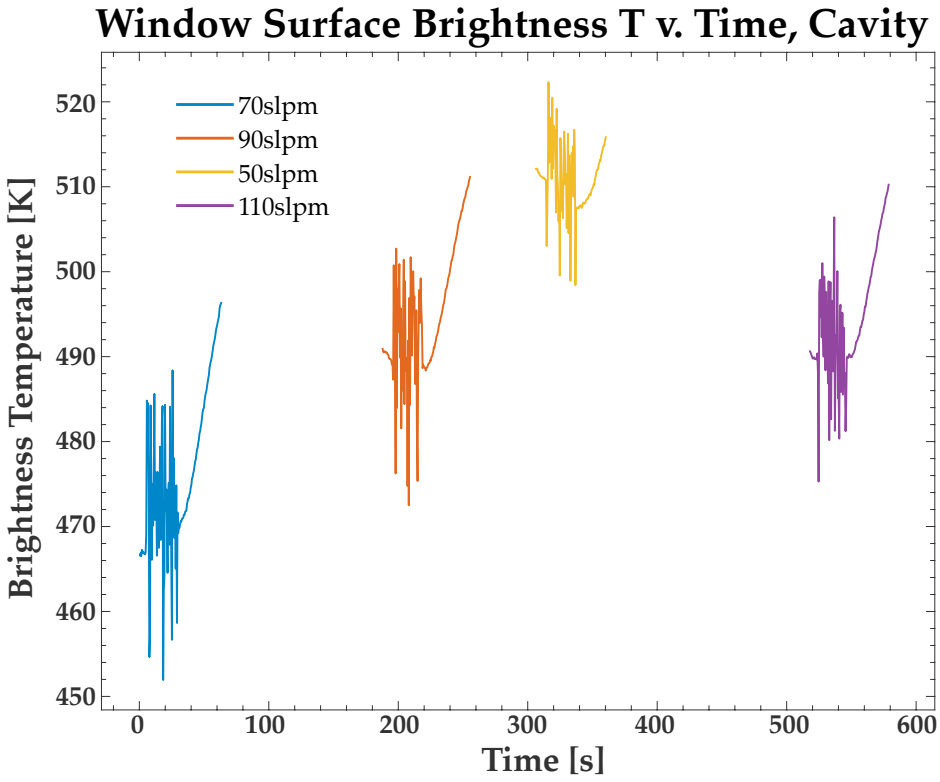

Figure 28. Temperature vs. time for Data Set 2 fueling runs

see a continual increase in temperature from the pre-burn data, carrying through to the post-burn data. This is consistent with the increase seen in Table 7, and is not surprising considering both the proximity of the pre-burn temperature to equilibrium, and that 70 sLpm delivers the greatest thermal impulse according to Table 3. The 90 sLpm run, in contrast, clearly has a downward trend in temperature immediately before the burn, and is slightly lower post-burn before heating becomes evident. The greatest drop in temperature between the pre and post burn data is captured in the 50 sLpm fueling rate, which is expected as the higher starting temperature will give greater strength to the cooling impulse delivered to the window as the cavity drops back to the temperature of the vitiated air. Thus, the subsequent thermal impulse delivered to the window by the combustion of the 50 sLpm fuel input will

www.manaraa.com

need additional time to overcome the cooling. Now considering the temperature data surrounding the 110 sLpm fueling rate, note that the pre-burn temperatures are significantly lower than those of the 50 sLpm fueling run, breaking the trend of continual temperature increase seen through the other three fueling rates. The pre-burn temperatures for the 110 sLpm rate has dropped to within five degrees of the pre-burn temperatures for the 90 sLpm fueling case. After the burn, however, there is a sharp increase in temperature with minimal temperature decrease prior to the upward turn. The significantly lower starting temperature of the 110 sLpm fueling condition can be partially explained by the slightly longer time-laps between it and the prior burn, however it is is more likely that our previous theory of the 50 sLpm fueling condition releasing significantly less energy is primarily responsible for the drop.

The uniform amount of data collected post-burn lead to fitting a section of the post-burn temperature for each fueling run to a line to better understand heating trends. These are reported in Table 8. Each fit was done with the same number of

Table 8. Window Surface Heating Rate for Each Fueling Rate

Fueling Rate	Post-Burn Line Slope [K/t]
70 sLpm	0.465
90 sLpm	0.375
50 sLpm	0.241
110 sLpm	0.385

data points taken over approximately 17 seconds of collection time. The number of data points to be included in the fit was determined by the 50 sLpm, which had the least amount of post-burn data. The subset of points chosen for the fit in each of the other fueling runs was chosen to start at the point where the post-burn data began

www.manaraa.com

to continuously increase. Note first the order of slopes from largest to smallest. At least two effects are influencing the values for these fitted rates. First, there is the amount of energy released into the window by the combustion. Greater energy release should be directly correlated to higher burn temperatures. Ordered by highest burn temperature and decreasing, the rates are 70 sLpm, 90 sLpm, 50 sLpm, then 110 sLpm. Comparing this order to the values reported in Table 8, we see this is not the case. Seeking an explanation, we return to our thermal heat transfer model, and recall that there is potentially a point when the window will approach thermal saturation, and as a result will respond less readily to a thermal impulse. Note that for this data set, the 70 sLpm fueling rate delivers its impulse at the lowest window temperature, while the 50 sLpm fueling rate does so at the highest temperature. If the window was experiencing some level of thermal saturation effects, we would expect the 70 sLpm to have the highest rate of heat transfer, the 50 sLpm to have the lowest, and the 90 sLpm and 110 sLpm to have comparable rates since they delivered their impulses at similar window temperatures. This matches the trends shown in Table 8 and thus is considered the most likely explanation.

Since the trends in this data set are well defined, we will also look at the trends of the window's surface brightness temperature for other spatial regions of the cavity, such as the metal and free stream. This will provide insight into the thermal transfer to other cavity elements. To generate these plots, the same method of averaging a subset of pixels viewing a particular cavity element to obtain a single temperature, then plotting these over time is utilized. Figure 29 shows the spatial regions over which the average was taken to produce the subsequent plots.

The region over the flame was used to produce the previous temperature vs. time plots. The spatial region to the left of the flame, in front of the metallic elements of the ramp, was chosen as it will provide insight into the heating of the metal cavity

www.manaraa.com

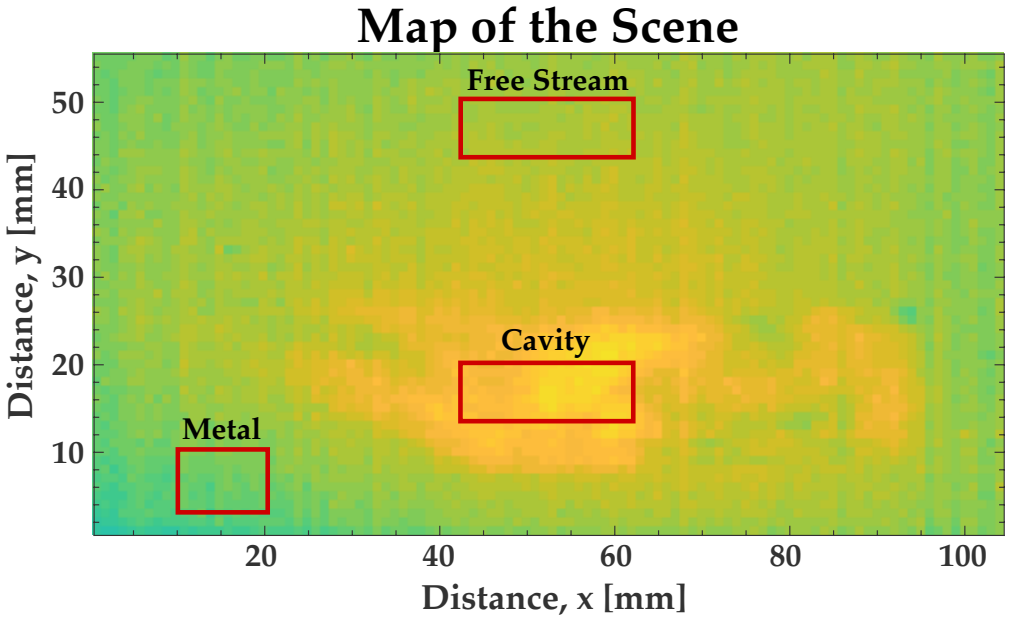

Figure 29. Three spatial regions averaged over to produce brightness temperature vs. time plots

elements. Since the window is in direct contact with only the metal in this area, the primary thermal impulse will come from the metal, though there will also be heating from other parts of the window. The region in the free stream was chosen as it will provide insights into the how the thermal impulse spreads to across the window. Since the area behind this region is being held at the temperature of the vitiated air, the only heating will come from the window itself since the flame is quickly swept down the tunnel if it rises outside the cavity. The temperature vs. time plots for the two additional spatial regions are shown in Figure 30. Note first that the large amount of noise that appeared in the region over the combustion cavity does not appear in either of these plots. Turning now to the plots generated from the metal region, notice first that the shape of these plots is very similar to those from over the combustion cavity, though the temperatures are lower here. Thus, more clearly evident is the

www.manaraa.com

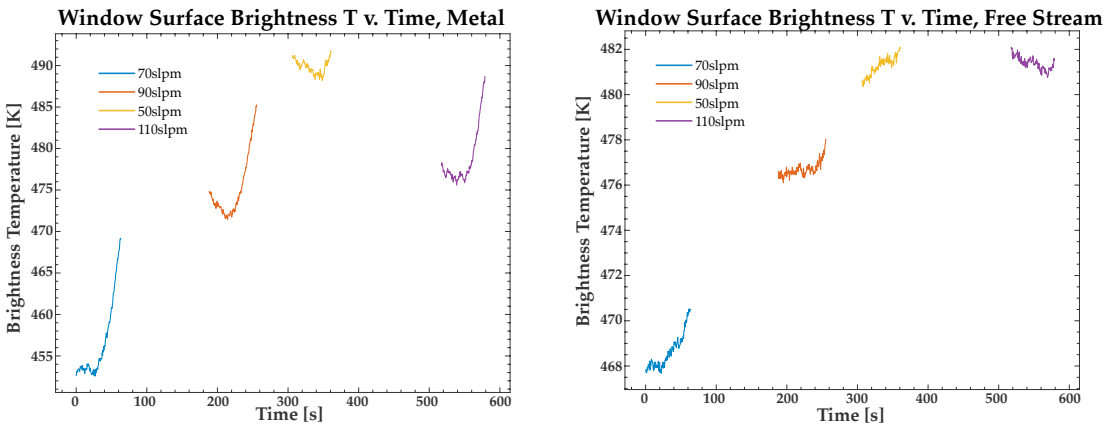

Figure 30. ***Left:*** **Temperature vs. time plots for a spatial region over metal.** ***Right:*** **Temperature vs. time plots for a spatial region over the free stream**

transition between cooling from contact with the vitiated air, and the heating from the combustion. The plots showing the temperature over the free stream have a very different shape, showing much slower increases in temperature with a smaller range of temperatures reached. Furthermore, no cooling trends are apparent until the 110 sLpm fueling rate. From these plots, there appears to be a slower but steady increase in temperature spreading across the window until the 50 sLpm fueling rate, at which point some cooling appears to take place. However, note at the beginning of the 110 sLpm fueling rate, the temperature has not decreases as much as it did in any of the other spatial regions. Here the temperature remains very close to the values achieved over the 50 sLpm fueling rate. At the end of the 110 sLpm data, there is a slight upward trend in temperature, indicating that heat released from the 110 sLpm burn is beginning to reach this region.

The data shown in Figure 30 shows that heat spreads much more quickly through the metal than the material of the window. This is as we would expect. It also confirms that the noise show over the burn region arrises from the combustion. We will now turn to consider these noise effects.

www.manaraa.com

4.3 Brightness Temperatures and Window Transmission Bands

Having explored the behavior of the temperature at the window surface, we now turn to consider what information can be gathered by looking through the spectral region where the transmission function of the window gradually increases. First, recall the transmission function of the window, shown in Figure 31.

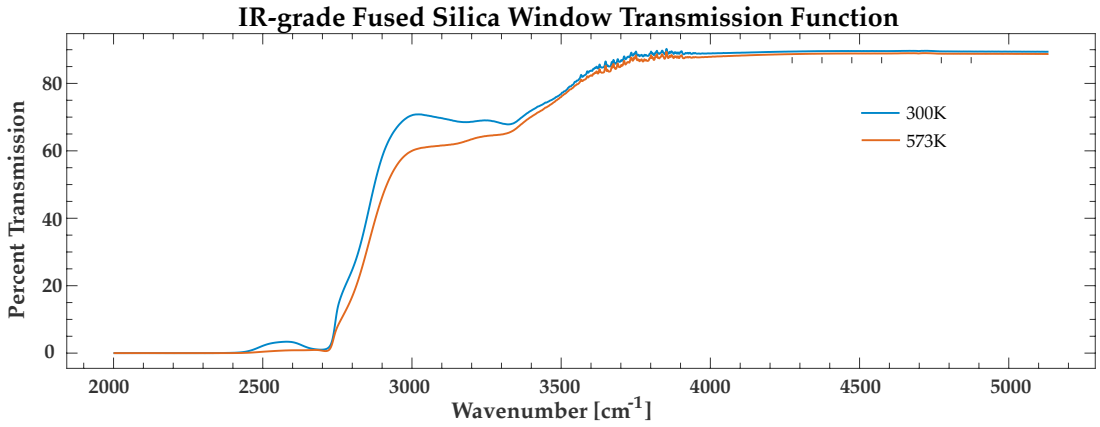

Figure 31. Spectral transmission function of the window at two different temperatures.

In the background section, it was shown how different layers of the window will contribute more or less radiance in different spectral bands. We expect as the window becomes more transparent, that radiance from layers farther back in the window will contribute more radiance directly to the camera. In Results Section 4.2, we saw that there was a time delay between the thermal impulse from the combustion being delivered to the interior of the window, and the heating of the outer window surface. It is possible that by looking at different spectral bands of the window, the propagation of the thermal impulse through the window could be observed. To test this theory, images of the window are taken and integrated over several spectral bands. For these images, data is taken from a single time point approximately 0.5 seconds after combustion has ended. At this point, the temperature gradient through the

www.manaraa.com

window should be significant, and radiance from the combustion will not overwhelm the emissions from the window itself. Figure 32 shows temperature maps for several spectral bands, and fueling rates taken from Data Set 2. Bands 1-5 in this image

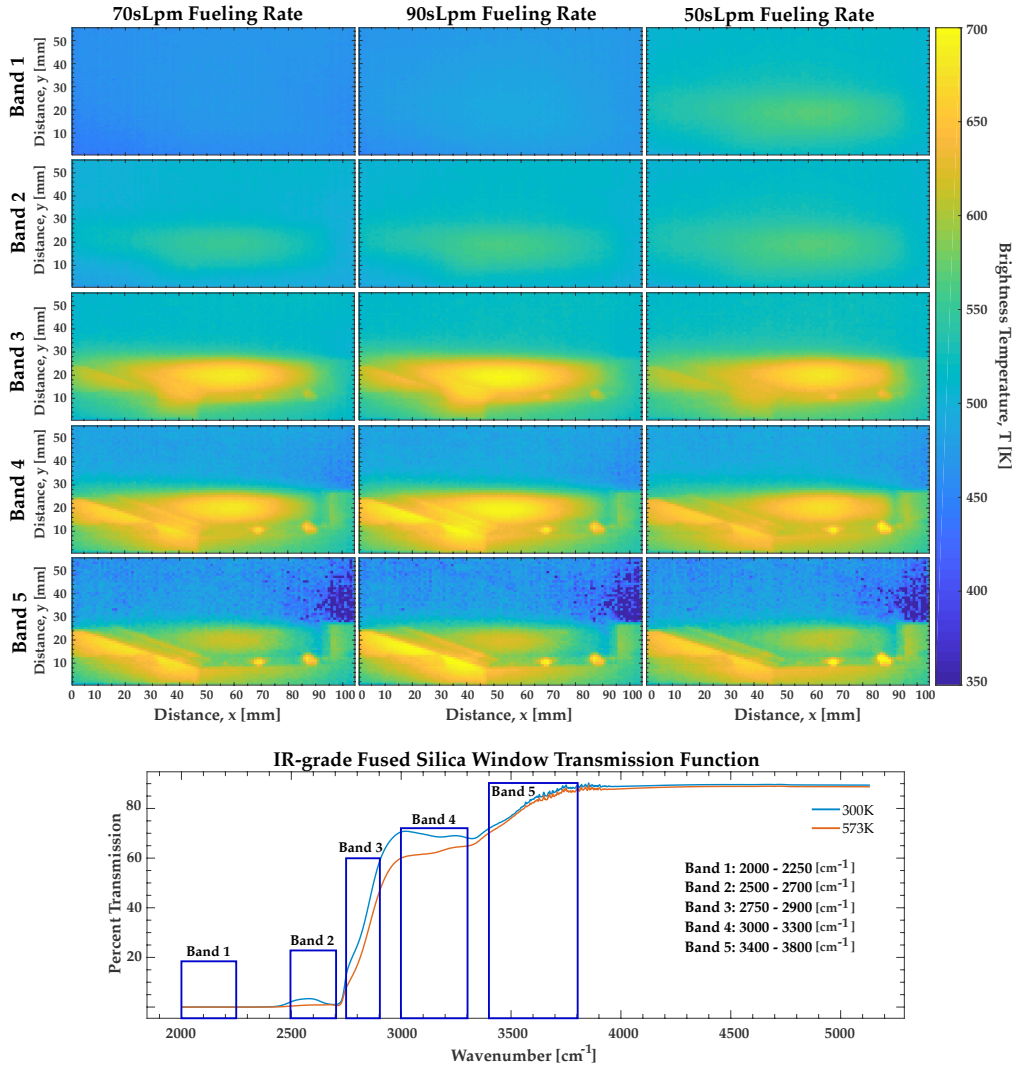

Figure 32. Brightness temperature maps for several spectral bands and fueling rates

progress from most opaque to most transparent. The temperature is lowest and most evenly distributed on the surface of the window in Band 1. In Band 2 the window's brightness temperature is higher, and what appears to be a warm region within the

www.manaraa.com

window is appearing over the combustion cavity. Since no combustion is currently occurring and there are not metallic elements behind this portion of the window, the observed emission must come from the window. In Band 3 the warm spot in the window has become significantly more distinct, and the metallic elements of the cavity are becoming visible. In Band 4 the warm spot has started to fade and the cavity elements become increasingly visible. Finally, in Band 5 all of the cavity is visible, but a dim warm spot on the window's inner surface is apparent.

These trends can further be observed by considering the progression of brightness temperature over time for each of the five representative spectral bands. These are shown for each fueling rate in Figure 33. Again, a spatial average of pixels viewing the

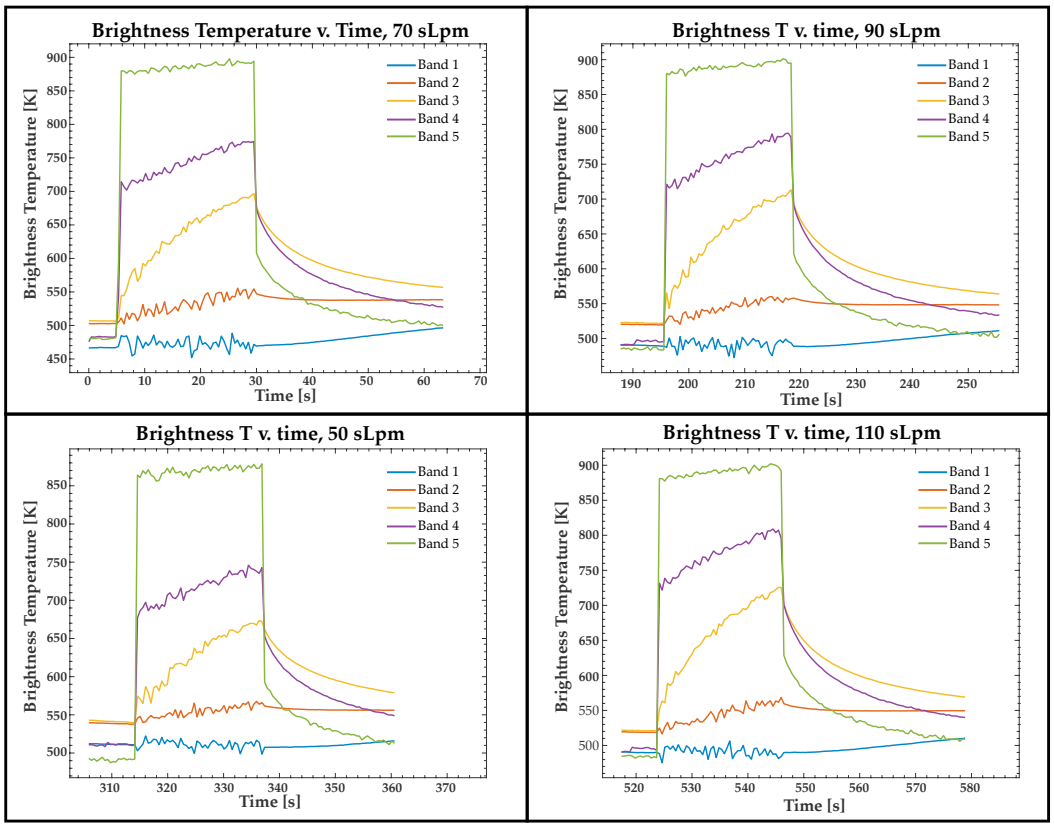

Figure 33. Brightness temperatures for different spectral bands

www.manaraa.com

combustion cavity is taken to produce each brightness temperature point in time. The trends shown in Band 1 have already been examined in previous sections. In Band 2 for all fueling rates, trends very similar to those of Band 1 are exhibited. However, the measured brightness temperature is higher, and the increase in temperature resulting from the thermal impulse of the burn occurs during the burn. Any post-burn increase in temperature is minimal, but rather the temperature holds to a stable value over the time post-burn data is collected. In Band 3 distinctively new trends become manifest. Once the burn begins, there is a small but distinct instantaneous jump in measured signal, which indicates that some signal from the flame itself is now being transmitted through the window. Throughout the burn there is a significant increase in temperature of at least 100°K for all fueling rates. Assuming that the temperature of the burn exhibits no substantial increase over the course of the burn, it can be concluded that the observed temperature increase results from heating of the internal window layers. This conclusion is strengthened by observing the post-burn data in Band 3. First note that this is the first band in which the post-burn data exhibits a downward or cooling trend. Observe however, after a small instantaneous downward jump (analogous to the upward jump at the beginning of the burn) the temperature drops off smoothly. Radiance from the flame is instantaneously extinguished, and thus would not cause this gradual downward trend. Thus, it is reasonable to conclude that the observed effect is from cooling of internal window layers. It is assumed that the cooling layers are primarily internal, as the data from surface of the window in Bands 1 and 2 show heating trends post-burn, therefore the cooling must occur behind these layers. At the beginning of the burn, Band 4's temperature has an instantaneous increase of at least 150°K for all fueling rates. During the burn, there is a gradual increase in temperature of 30-50°K for all fueling rates indicating that some window heating effects are manifest, though more of the signal from the flame

www.manaraa.com

is being transmitted here than in Band 3. After the burn, there is a instantaneous downward jump immediately after the flame is extinguished followed by a cooling curve that falls more rapidly than the one in Band 3. This indicates that the window layers primarily contributing to this signal are behind through contributing to Bands 1,2, and 3. At this point it is possible that the cooling of the back window is also contributing to the signal. Finally, Band 5 shows the largest instantaneous change in temperature before and after the burn, being at least 250°K change for all fueling rates, indicating the primary signal source in this band is the flame. After the burn, some cooling effects are still evident, having a profile very similar to the one seen in Band 4 with a downward offset of 30-50°K. This indicates that window effects are still evident in the spectra range captured in Band 5. However, the radiance contributions from the window in this band is less that that of the previous bands, and a spectral range is now being approached where window effects can be considering negligible.

It should be noted and recalled from the background that the brightness temperatures calculated and shown in Figure 32 do not show the true thermal temperature for a particular layer within the window. Unlike in the case of the opaque spectral region, radiance emissions are not limited to a particular optical plane. Rather, radiance from many different optical depths are contributing the radiance used to calculate the brightness temperature, and as the transmission function increases there is no way to limit contributions to a single optical plane. Thus, the trends rather than quantitative values are what can be currently mined from the data.

It is desirable to employ our models to provides more quantitative context to the trends observed in these different spectral bands. As an initial effort to achieve this goal, consider the full spectra taken from the same post-burn frame used to create the brightness temperature maps shown in Figure 32. The spatially averaged spectra for each fueling rate is shown in Figure 34. First, note that the trends exhibited in

www.manaraa.com

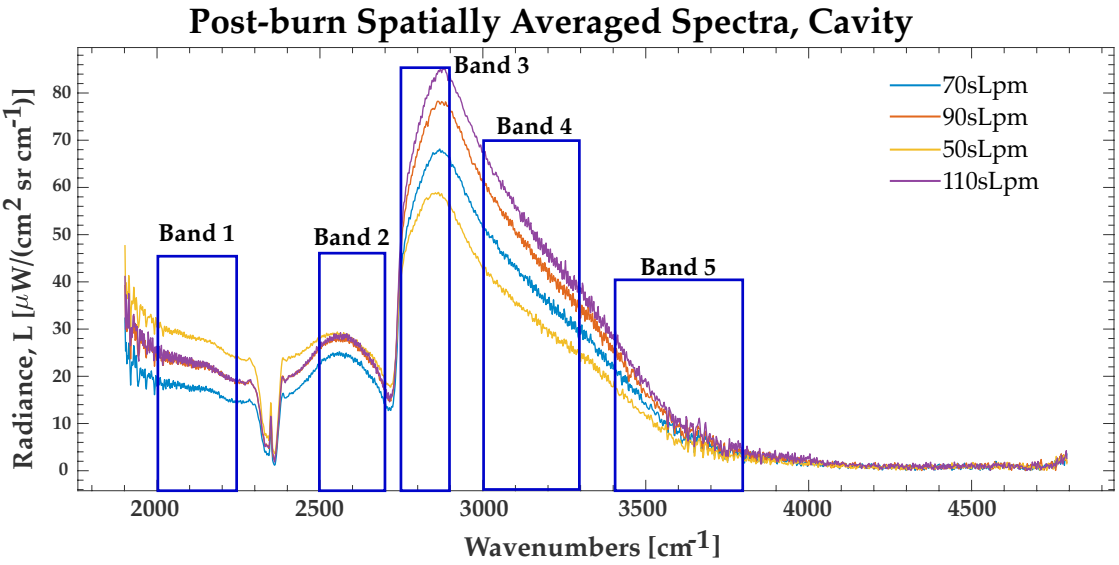

Figure 34. Spectra generated from the spatial region over the cavity. Taken approximately 0.5 seconds post combustion for each fueling condition

the spectra match those shown in Figure 32, with the radiance levels over the cavity increasing through Bands 1 and 2, peaking in Band 3 then decreasing through Bands 4 and 5. Furthermore, in Bands 1 and 2 the 50 sLpm has the highest radiance level with 70 sLpm being the lowest. However, once Band 3 is reached, the order changes with 110 sLpm being the highest, followed by 90 sLpm, 70 sLpm, and 50 sLpm. These are also consistent with the trends observed in Figure 32.

Since the spectra shown in Figure 34 is taken from a post-burn frame and averaged over the cavity region, it can be assumed that window effects are the primary contributor. Thus, the spectra show provides a spectra profile of window emissions, contributed by various window layers at each spectral location. Recall now the formulation of weighting functions given in the Background. The primary equation used to perform this analysis is given in Equation 18 for reference.

$$L(\tilde{\nu}, d) = L_0 \tau_w(\tilde{\nu}, d) + \int_0^d B(\tilde{\nu}, T(s'))W(\tilde{\nu}, s')ds' \tag{18}$$

www.manaraa.com

To gain insight into what the weighting functions predictions for window layer contributions, both W as a function of window depth for each band, and W as a function of wavenumber for the total window depth. Figure 35 provides a concise display of all the information necessary to evaluate the use of the weighting function. First,

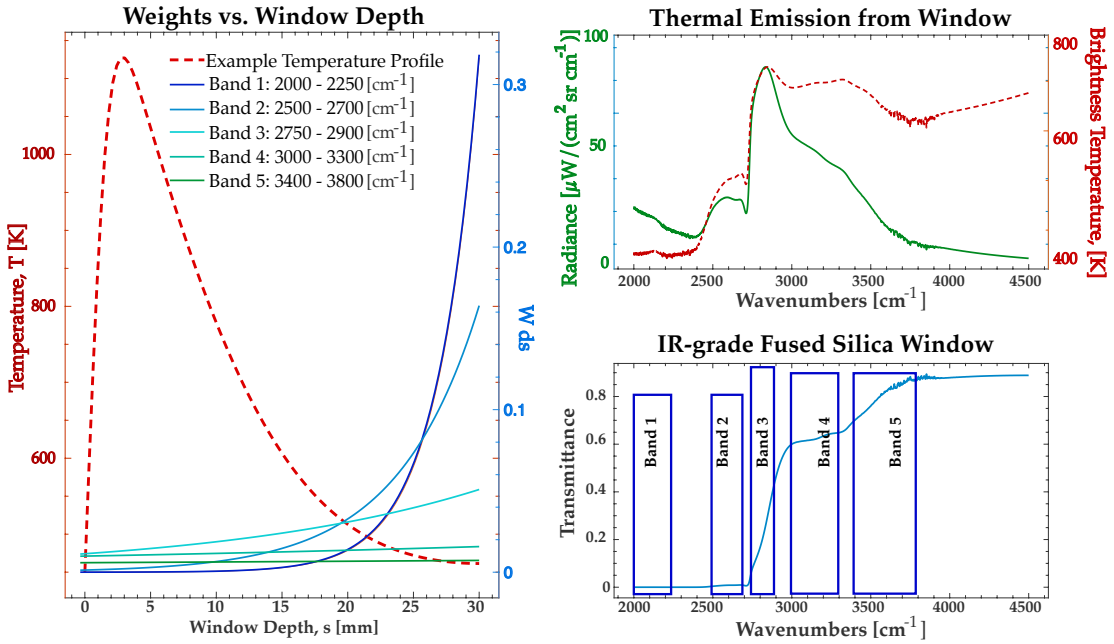

Figure 35. ***Left*: The weighting functions across window depth for each spectral band is displayed. Also plotted is an example temperature profile of the window depth.** ***Right, Top*: The emission profile of the window generated from the weighting function and the example temperature profile is plotted both in radiance values and brightness temperature.** ***Right, Bottom*: The transmission function of the window with the five representative spectral bands used for analysis is plotted for reference.**

consider on the left weighting functions over window depth for each of the five representative spectral bands. In Band 1 and Band 2, radiance contributions from the surface of the window dominates. Weighting function values for window layers from zero to 10 mm are below 0.005 for both bands, while contributions from 29 to 30mm are approximately 0.3 and 0.15 respectively. Furthermore, the weighting functions

www.manaraa.com

for these two bands exhibit an exponential shape. In contrast, the weighting function from Band 3 exhibits a slow linear increase as it goes from the interior to exterior surface of the window while Band 4, and Band 5 and almost flat-lined at a very low Wds value. In both these cases the window layers are contributing to the total radiance, though this contribution becomes smaller for each band.

Observation of these trends is helpful, but referencing back to Equation 18, note that the radiance profile of the window is formed by multiplying the weighting function by the blackbody profile $B(\tilde{\nu}, T(s'))$ for a particular temperature profile $T(s')$. Note the temperature profile plotted in red with the weighting functions. At the surface of the window, the temperature is low and slowly increases through the outer half of the window. As the interior surface of the window is approached, however, there is a sharp increase in in temperature which then sharply drops off when the interior window surface is finally reached. It appears that the temperature at a particular window depth will be a very strong driving function for how much radiance is observed from a particular window layer. This theory is verified when we consider that within the data reported, the greatest radiance emissions were given by Band 3, even though the weighting function is lower for this band. This is because the the layers of highest temperature become visible.

To form a prediction of the radiance profile of the window using the weighting functions and our example temperature profile, we calculate the term $\int_0^d B(\tilde{\nu}, T(s'))W(\tilde{\nu}, s')ds'$ from Equation 18, disregarding the $L_0\tau_w(\tilde{\nu}, l)$ as it can be considered as a offset, not effecting the shape. The result of this is shown in the top right image in Figure 35. Note that this predicted emission profile is generated by integrating over the full depth of the window, thus all layers are captured. Also plotted is the same profile converted to brightness temperature. Note first that the trends observed in each of the five bands (displayed over the transmission function in the bottom right image)

www.manaraa.com

match what was observed in the data. The brightness temperature is particularly helpful in making comparisons to the maps shown in Figure 32.

This predicted profile for the window emission shown in Figure 35 seems to match the trends exhibited in Figure 34. The predicted and measured profiles are explicitly compared in Figure 36. From this comparison, it is evident that the spectra generated

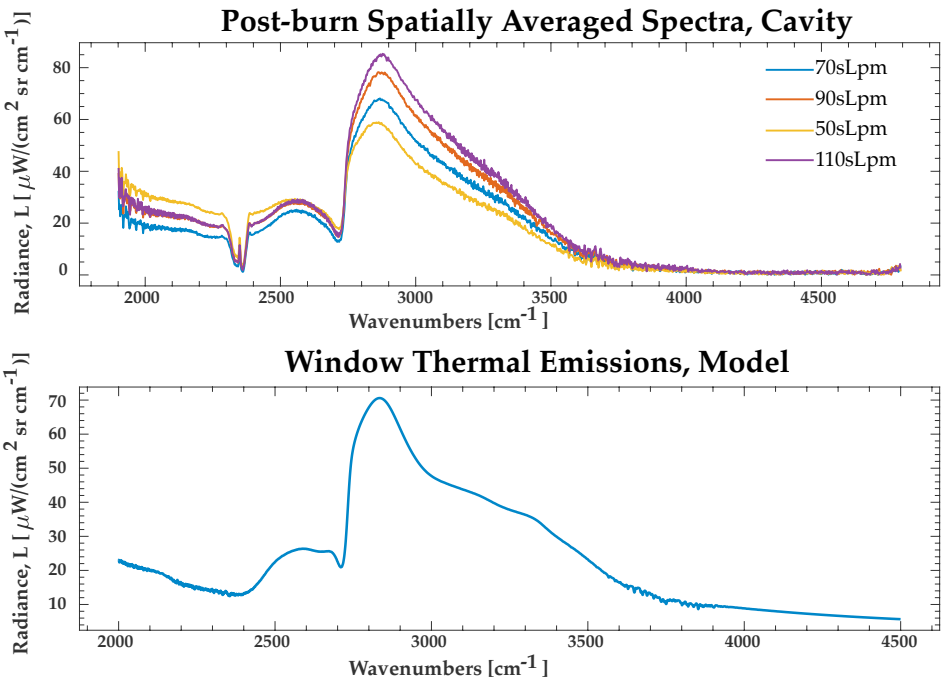

Figure 36. Comparison of measured spectral emission profiles from the window with model's prediction for the profile.

by the model closely matches the measured spectra for the window profile. This analysis illustrates a method that could be used to calculate the radiance contributions, and thereby the temperature, of each layer of the window. The weighting functions used in Equation 18 are only dependent on the transmission function of the window and optical constants of the material, which can be measured with high precision. Using an approximation for the background radiance L_0 post combustion, and tak-

www.manaraa.com

ing the measured values at the total output radiance, only remaining unknown in Equation 18 is the temperature of each window layer $T(s')$, thus making it possible to solve for these temperatures and determine the radiance contributions from the window over the spectral range of the instrument.

This work does not contain an attempt to solve for these temperatures, as dependable values for the optical constants and transmission function for the window at high temperatures are not yet available. However, once these material properties are known with confidence, solutions for the temperature profiles could reasonably be attained using the methods and results previously described.

4.4 Turbulence and Noise

In both the temperature maps taken during the burn and the temperature vs. time plots generated by a spatial average taken over the cavity, there are significant signal fluctuations caused by the combustion. This fluctuation is very large, pushing the signal sometimes far above and sometimes far below the apparent baseline signal. The theoretical basis for this phenomenon was given in the background section. This can make a baseline signal difficult to discern, and great care must be taken in any attempt to mitigate these fluctuations for multiple reasons. First, the extreme range of the fluctuations lead to negative signals being recorded. Over the process of analyzing the data, these negative signals can create a false positive bias in the reported signal levels. Thus, care must be taken in selecting the point in the data analysis process that the fluctuations are treated, and the method used. Second, any attempt to treat the signal fluctuations caused by the turbulence as "simply noise" ignores the very physical cause of this phenomena. The combustion cavity is an extremely turbulent environment, and the fluctuations in the signal captures this phenomena

www.manaraa.com

of turbulence. Interpretation of this signal fluctuation to something physical about the turbulence may be challenging, but information about the turbulence is captured in this fluctuation. An attempt will now be made to characterize the turbulent sig-

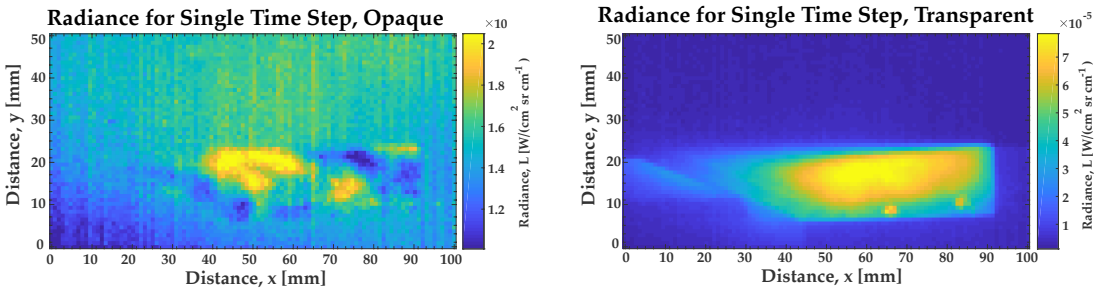

Figure 37. Radiance map of a single cube taken in the middle of the burn.Spectral average over 2000-2250 cm^{-1} and 2500-5000 cm^{-1} respectively.

nal fluctuations, potentially paving the way for further quantitative analysis. First, consider the radiance maps taken during the 70 sLpm fueling rate from Data Set 2, shown in Figure 37.

The left side of Figure 37 shows the radiance emitted where the window is opaque, while the right side of Figure 37 shows the radiance emitted in the spectral band where the window is transparent. Both of these images are taken from a single time step in the middle of the burn. Notice how different the radiance profiles in either images appears. The the image in the opaque spectral range shows regions of both high and low radiance within the combustion cavity, and no cavity elements are visible. In contrast, the image in the transparent spectral range shows a consistently bright area where the flame is burning, and cavity elements such as the ramp and hot probes on the base of the cavity are clearly visible. In the region where the window is transparent we know that the primary radiance contributions will be from the flame, while where it is opaque any radiance emitted by the flame will have to be absorbed by the window before being reemitted. By comparing the two images in Figure 37, we

www.manaraa.com

can concluded that the strange fluctuations from the left hand image do not arrises directly from the radiance of the flame. The shape of the of the cavity emissions in the left image do not match those of image on the right, and locations of the bright spots are not aligned.

From this, it can be postulated that the fluctuations seen arise directly from the turbulence, as shown in the background. It cannot be determined from these images,however, what signals arise solely from turbulence and which are from the radiance emission of other elements. It would be of interest to look at the cavity where the only signal measured is contributed by turbulent fluctuations, thereby allowing observation of the regions of greatest turbulence at particular frequencies, and the relative strength. This can be accomplished by considering the raw data, and the spectral regions outside of the camera bandpass. Consider the raw spectral shown in Figure 38. The spectra shown was taken from a single pixel in the center

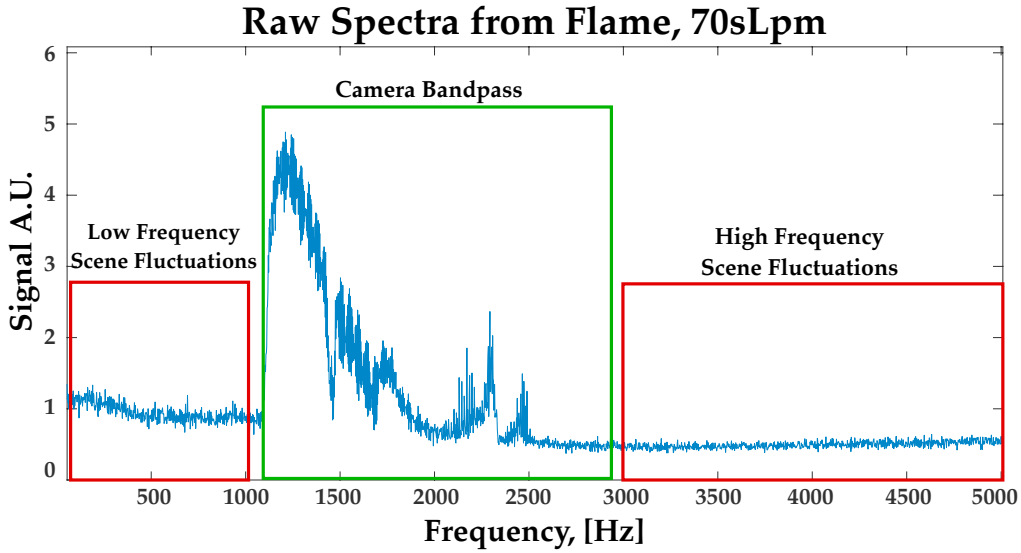

Figure 38. A raw, time-averaged spectra taken from a single pixel of the data from Data Set 2's 70 sLpm burn

www.manaraa.com

of the cavity region, and is the time-average of all cubes taken during the 70 sLpm burn in Data Set 2. This spectra is uncalibrated, and shows both signal from within the camera's bandpass, and from regions where the FPA is not sensitive but the instrument is still capable of recording information. These regions are approximately marked. As explained in the background, for a stable scene without fluctuations, the raw signal will be zero outside of the camera's bandpass. If the scene is changing, however, the frequencies at which this change occurs will be recorded in the sampling regions both inside and outside the camera's bandpass. Within the camera bandpass, separating what signal arrises from the scene fluctuations and which are from scene radiance is a difficult task. If however, an image were made by integrated the raw spectra on either side of the camera bandpass, one could be confident that the only recorded signal arrises from scene fluctuation. Images resulting from integrating raw spectra over the high and low frequency bands depicted in Figure 38 for Data Set 2's 70 sLpm fueling rate are shown in Figure 39. None of the signal shown in these maps comes from radiance emissions from the cavity, rather, all signal comes from frequency fluctuations. However, the moving elements must be emitting some signal to be detected by the IFTS. The upper image shows the fluctuations at frequencies below the camera bandpass and the the lower image shows frequency fluctuations above the camera bandpass. Note that these images do not show all the fluctuations of the flame, there are also fluctuations that appear in the camera's bandpass region, and others that are not detectable with this instrument. However, integrating over these regions, some interesting trends become apparent. First, notice that the signal from the low frequency fluctuations is just under three times higher than the signal from the high frequency fluctuations, indicating that there is more turbulence in the lower band than the higher one. Also notice that the distribution of the turbulence through the cavity is distinctly different for the two cases. In the high frequency

www.manaraa.com

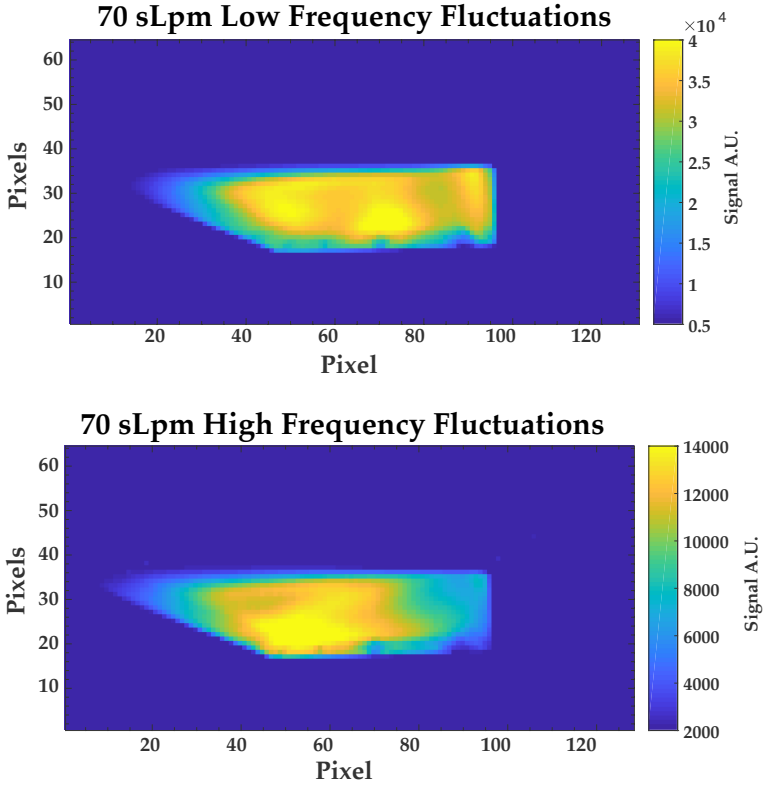

Figure 39. Maps of the high and low frequency fluctuations in the flame.

case, the turbulence is concentrated at the point that the base of cavity meets the ramp, which is very close to the fuel injection point. There is also a slightly great turbulence concentration along the shear layer above the ramp. In contrast, in the lower frequency case the turbulence is more evenly distributed through the cavity, with three areas of higher concentration by the shelf, in the center of the cavity floor, and approximately halfway up the ramp.

A final comparison that can be made of high and low frequency fluctuations is by comparing them for all the fueling rates tested in Data Set 2. Figure 40 shows this comparison. It is evident that there are significant differences in fluctuation for the different fueling rates. In the lower frequency range, as we move from lower to

www.manaraa.com

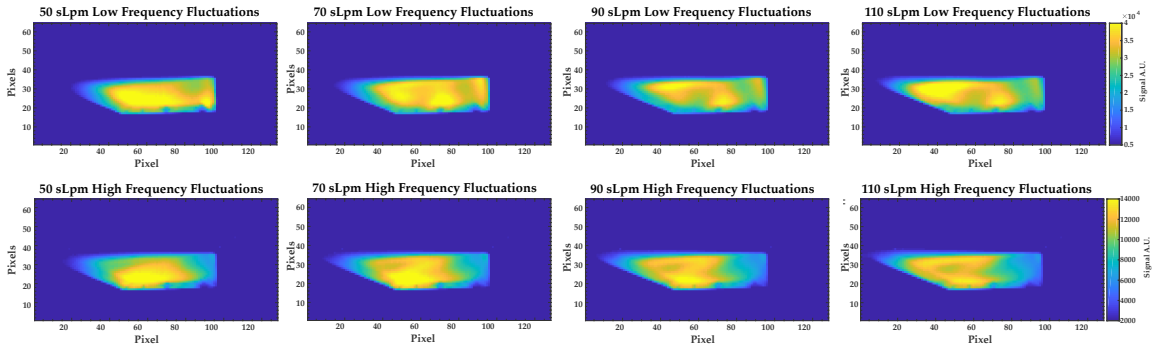

Figure 40. Comparison of high and low frequency fluctuations for all fueling rates

higher fueling rates the area of greatest fluctuation progresses from being distributed throughout the cavity to being primarily concentrated on the ramp above the fuel injection point. In the high frequency range, the progression from lower to higher fueling rates show turbulence moving from being concentrated primarily at the point where the base of the cavity meets the ramp at the fuel injection point, to appearing progressively more in the shear layer while decreasing in concentration at the injection point.

Apparently, fueling rates can be differentiated between by considering the distribution and concentration of frequency fluctuation outside the camera bandpass. Determining the quantitative connection between these measurements and the physical characteristics of the flame is beyond the scope of this work. However, one can conceived that a calibration scheme could be contrived to convert this arbitrary signal into meaningful units. Furthermore, it is possible that different particles within the flame, such as combustion byproducts, will tend to fluctuate in different frequency bands based on physical parameters such as size and mass. Further research would be needed to confirm any of these theories, however they provide potential avenues for additional investigation.

www.manaraa.com

V. Conclusions

5.1 Summary of Results

The first trends examined in the results section was the brightness temperature associated with the window's outer surface. Since the transmission function was very close to zero in the spectral band integrated over for these results, measured signal was assumed to be emitted from a single optical plane. Because of this, it was reasonable to assume brightness temperature calculations provided a good approximation of the true surface temperature. Observations were made of the baseline starting temperature of the window, and the gradual increase in temperature as successive fueling conditions were ignited. The time needed for the thermal impulse caused by the combustion to travel to the surface of the window was explored. Conjectures were also made concerning the connection between the maximum window temperature observed after a fueling run, and they amount of energy released during that run. It was concluded that the absolute peak temperature after the burn was never observed, additional data would have to be collected to continue that line of inquiry.

Following this, several bands with varying window transmission levels were taken together with the purpose of parameterizing the effects of the window contributions on the measured signal over the bandpass of the camera. Focusing initial efforts on data that had been taken immediately after the flame was extinguished, it was observed the thermal impulse from the combustion created a thermal distribution across the window that was consistent with the predictions of the one-dimensional transfer model. A radiative transfer model was then used to predict the radiance contribution from each window layer for each spectral band. A method for finding the temperature distribution across the thickness of the window was outlined, thought

www.manaraa.com

better measurements of the material properties of the window would be required to predicted the temperature distribution. Further data representations were used to explore the window contributions from different perspectives.

Finally, the cause of significant noise fluctuations during the burn were explored. It was observed that the scene fluctuations caused by the extremely turbulent conditions effected the measured signal in all spectral channels across the camera bandpass. Examination of the raw spectra showed that these these turbulence fluctuations were also captured outside the camera bandpass across all frequencies the instrument was capable of resolving. By integrating over the frequency ranges above and below the bandpass, images were produced showing spatially resolved regions of high and low frequency fluctuation within the flame. With a better understanding of the signal, these images could be of use to CFD efforts.

Highlighted by the various data representations throughout this work is the IFTS capabilities as a diagnostic instrument for turbulent scenes. The capture of spatially resolved, broadband spectral data over time provided a way for many trends to be observed for a single data set. Furthermore, the interferometric system, generally considered a hindrance in capture of turbulent data, enabled the production of a spatially resolved map of the turbulence fluctuations for the frequencies captured outside the camera bandpass. This provides additional conformation of the IFTS value to combustion diagnostic efforts.

5.2 Contributions to Previous and Current Research Efforts

In previously accomplished work, the effects of the window on measurements and subsequently results was not well understood. The analysis provided in this work

www.manaraa.com

confirms that the results produced elsewhere were indeed within the spectral bands where the window emission effects were small, and could reasonably be approximated as an offset. Having this conformation strengthens the basis on which prior work was built and will enable a higher level of confidence for similar efforts done in the future.

In addition to this, the information captured in the spectral bands influenced strongly by window effects provide a means for several valuable contributions to CFD modeling efforts. There are two primary ways in which this research contributes to CFD calculations. The first is by providing physical parameters that can serve as inputs. The method developed here for estimating the temperature across the interior surface of the viewing window before and after the burn provides boundary layer conditions for the CFD models. Furthermore, the estimates of the temperature distribution through the thickness of the viewing window provides a means by which temperature boundary layer conditions during the burn can be estimated. The second significant contribution to CFD is the provision of dependable results that can be compared to CFD outputs. For example, given our understanding of the window effects, it is now conceivable to integrate the CFD modeling outputs over the line of sight that was measured by our instrument and compare them to the measured results. This can be done both for the radiance measurement, and for the turbulence measurements shown in the results. The higher dependability of CFD results can lead to insights in interpretation of the data collected by our IFTS system. The inputs used to generate the CFD model results can provide additional knowledge of the physical processes contributing to our measurements, and lead to new ways of analyzing and processing the results. Eventually, it is our hope that a strong synergetic relationship will be established between IFTS diagnostics and CFD.

www.manaraa.com

5.3 Future Work

The results presented in this work primarily focused on the analysis of qualitative trends without many quantitative conclusions. However, many of these trends can lead to quantitative results with additional efforts. Three realms of future work present themselves. The first and arguably the most important is measurements of material and optical constants in which we can be fully confident. It may be that additional measurements of these material properties at high temperatures for the IR grade fused silica viewing window are necessary. Performing a sensitivity analysis to ascertain the effect of the optical constants on our models would be a reasonable starting point to determining the precision necessary to have a high level of confidence in our models. This subsequently would lead to the development of more robust radiative and thermal heat transfer models that would provide a basis on which to begin exploration of the interior of the cavity in novel ways. A final reasonable effort would be to attach a thermal couple to the exterior window surface during combustion to determine the accuracy of the temperatures calculated using the brightness temperature conversion.

Additional exploration of the frequency regions outside of the camera bandpass focused on converting the raw signal to some physically meaningful units could have significant effects on exploration of scramjet cavity turbulence.

A final additional effort that could lead to novel results is continuous data capture during the combustion of several fueling conditions. The resulting observations that could be made of window heating and cooling could lead to insights into the energy release and heat propagation through the cavity for different fueling rates. In support

www.manaraa.com

of this, a 3-D heat transfer equation should be developed to effectively utilize the processing of additional data.

www.manaraa.com

Bibliography

[1] Michael R. Rhoby. *Laminar Flame Combustion Diagnostics Using Imaging Fourier Transform Spectroscopy*. PhD thesis, AFIT, 2016.

[2] T. Ombrello, D. Blunck, and M Resor. Quantified infrared imaging of ignition and combustion in a supersonic flow. *Experiments in Fluids*, 57:140, 2016.

[3] M. R. Rhoby, A. M. Kerst, K. C. Gross, and T. M. Ombrello. Hyperspectral imaging diagnostics of a scramjet combustor cavity. In *10th U.S National Combustion Meeting, Combustion Institute*, 2017.

[4] Michael R. Rhoby, David L. Blunck, and Kevin C. Gross. Mid-IR hyperspectral imaging of laminar flames for 2-D scalar values. *Optics Express*, 22(18):21600 – 21617, 2014.

[5] M.A. Bolshov, Yu.A. Kuritsyn, and Yu.V. Romanovskii. Tunable diode laser spectroscopy as a technique for combustion diagnostics, 2015.

[6] M. Aldén, J. Bood, Z. Li, and M. Richter. Visualization and understanding of combustion processes using spatially and temporally resolved laser diagnostic techniques. volume 33(1):69-97, P.O. Box 118, S-221 00 Lund, Sweden, 2011. Division of Combustion Physics, Lund University, Elsevier Inc.

[7] Wolfrum J. Lasers in combustion: From basic theory to practical devices. In *Proceedings of the Combustion Institute*, volume 27, pages 1–41, 1998.

[8] Kohse-Hoinghaus K. Laser techniques for the quantitative detection of reactive intermediates in combustion systems. *Progress in Energy and Combustion Science*, 20(3):203–279, 1994.

[9] Richter D. Fried A. *Infrared Absorption Spectroscopy, in Analytical Techniques for Atmospheric Measurment*. Blackwell Publishing, 2007.

[10] P. Lee, B. McMillin, J. Palmer, and R. Hanson. Planar fluorescence imaging of a transverse het in a supersonic crossflow. *Propuls. Power*, 8:729–735, 1992.

[11] M. Allen, T. Parker, and Reinecke. Fluorescence imaging of oh and no in a model supersonic combustor. *AIAA Journal*, 31:505–512, 1993.

[12] M. Gruber, J. Donbar, C. Carter, and K. Hsu. Mixing and combustion studies using cavity-based flameholders in a supersonic flow. *Propuls. Power*, 20:769–778, 2004.

[13] Combustion Institute. *Planar Laser-induced Fluorescence Imaging of OH in a Supersonic Combustor Fueled with Ethylene and Methane*, volume 32, 2009.

www.manaraa.com

[14] V. Kobtsev, D. Kozlov, S. Kostritsa, V. Smirnov, and A. Stel'makh, O. andTumanov. Laser spectrometric measurement system for local express diagnostics of flame at combustion of liquid hydrocarbon fuels. *Optics and Spectroscopy*, 120:492–499, March 2016.

[15] Gonzalez-Cencerrado A. and Gil A. Peña B. Coal flame characterization by means of digital image processing in a semi-industrial scale pf swirl burner. *Applied Energy*, 94:375–384, 2012.

[16] Allouis C., Pagliara R., and Saponaro A. Fast infrared imaging for combustion stability analysis of industrial burners. *Experimental Thermal and Fluid Science*, 43:2–8, 2012.

[17] Ehn A., Johansson O., Bood J., Arvidsson A., Li B., and Aldén M. Fluorescence lifetime imaging in a flame. In *Proceedings of the Combustion Institute*, volume 33, pages 807–813, 2011.

[18] Jainski C., Lu L., Dreizler A., and Sick V. High-speed micro particle image velocimetry studies of boundary-layer flows in a direct-injection engine. *International Journal of Engine Research*, 14:247–259, 2013.

[19] Sick V. High speed imaging in fundamental and applied combustion research. In *Proceedings of the Combustion Institute*, volume 34, pages 3509–3530, 2013.

[20] Vattulainen J., Nummela V., Hernberg R., and Kytölä J. A system for quantitative imaging diagnostics and its application to pyrometric in-cylinder flame-temperature measurements in large diesel engines. *Measurement Science and Technology*, 11:103–119, 2000.

[21] Huang H. and Zhang Y. Flame colour characterization in the visible and infrared spectrum using a digital camera and image processing. *Measurement Science and Technology*, 19, 2008.

[22] Ji J., Gore J., Sivathanu Y., and Lim J. Fast infrared array spectrometer with a thermoelectrically cooled 160-element pbse detector. *Review of Scientific Instruments*, 2004.

[23] Mooney J., Vickers V., An M., and Brodzik A. High-throughput hyperspectral infrared camera. *J. Opt. Soc. Am. A*, 1997.

[24] Jacob L. Harley, Brent A. Rankin, David L. Blunck, Jay P. Gore, and Kevin C. Gross. Imaging fourier-transform spectrometer measurements of a turbulent non-premixed jet flame. *Optics Letters*, 39(8):2350–2353, 2014.

[25] K. C. Gross, P. Tremblay, K. C. Bradley, M. Chamberland, V. Farley, and G. P. Perram. Instrument calibration and lineshape modeling for ultraspectral imagery measurements of industrial smokestack emissions. *Proceedings of SPIE*, 7695(769516), 2010.

المنارة للاستشارات
www.manaraa.com

REPORT DOCUMENTATION PAGE

Form Approved
OMB No. 0704–0188

The public reporting burden for this collection of information is estimated to average 1 hour per response, including the time for reviewing instructions, searching existing data sources, gathering and maintaining the data needed, and completing and reviewing the collection of information. Send comments regarding this burden estimate or any other aspect of this collection of information, including suggestions for reducing this burden to Department of Defense, Washington Headquarters Services, Directorate for Information Operations and Reports (0704–0188), 1215 Jefferson Davis Highway, Suite 1204, Arlington, VA 22202–4302. Respondents should be aware that notwithstanding any other provision of law, no person shall be subject to any penalty for failing to comply with a collection of information if it does not display a currently valid OMB control number. **PLEASE DO NOT RETURN YOUR FORM TO THE ABOVE ADDRESS.**

1. REPORT DATE *(DD–MM–YYYY)*	2. REPORT TYPE	3. DATES COVERED *(From — To)*
02–05–2018	Master's Thesis	1 July 2016 - 1 June 2018

4. TITLE AND SUBTITLE

Investigation of Scramjet Flowfield Temperatures at the Boundary Layer with Hyperspectral Imaging

5a. CONTRACT NUMBER

5b. GRANT NUMBER

5c. PROGRAM ELEMENT NUMBER

6. AUTHOR(S)

Amy M. Kerst

5d. PROJECT NUMBER

18P293

5e. TASK NUMBER

5f. WORK UNIT NUMBER

7. PERFORMING ORGANIZATION NAME(S) AND ADDRESS(ES)

Air Force Institute of Technology
Graduate School of Engineering and Management (AFIT/EN)
2950 Hobson Way
WPAFB OH 45433-7765

8. PERFORMING ORGANIZATION REPORT NUMBER

AFIT-ENP-MS-18-J-011

9. SPONSORING / MONITORING AGENCY NAME(S) AND ADDRESS(ES)

Air Force Office of Scientific Research
Dr. Chiping Li, AFOSR/RTA1
875 N. Randolph, Ste.325
Arlington Virginia, 22203
1 (703) 696-7797

10. SPONSOR/MONITOR'S ACRONYM(S)

AFOSR

11. SPONSOR/MONITOR'S REPORT NUMBER(S)

12. DISTRIBUTION / AVAILABILITY STATEMENT

APPROVED FOR PUBLIC RELEASE; DISTRIBUTION UNLIMITED.

13. SUPPLEMENTARY NOTES

14. ABSTRACT

Within the domain of chemical propulsion, the fields of combustion diagnostics and computational fluid dynamics each have a long history, and both have led to a better understanding of complex phenomena yielding practical improvements in propulsion systems. As more exotic forms of propulsion are developed, the importance of both diagnostic and simulation capabilities also increase. In the case of scramjet combustion, these challenges primarily arise from the highly turbulent environment in the combustion cavity, and the high-speed, compressible nature of the flowfield. Efforts are underway to develop computer models of scramjet combustion environments to better understand the evolution of the flow field and heat transfer to the walls during combustion. This thesis effort experimentally supports these goals. Specifically, hyperspectral imaging measurements of an optically accessible scramjet were collected for different fueling rates. The primary focus was characterization the magnitude and dynamics of the outer window temperature in its response to combustion of different fueling rate. The window represents an important and dynamic boundary condition, and these hyperspectral measurements could be used to validate numerical simulations. Other work in this thesis effort explores qualitative differences in flowfield turbulence under different fueling conditions, and in principle this turbulence characterization could also be used to for comparisons with numerical simulations.

15. SUBJECT TERMS

Imaging Fourier-Transform Spectrometer, Hyperspectral Imaging, Combustion, Scramjets, Radiative Transfer, Thermal Heat Transfer

16. SECURITY CLASSIFICATION OF:			17. LIMITATION OF ABSTRACT	18. NUMBER OF PAGES	19a. NAME OF RESPONSIBLE PERSON
a. REPORT	b. ABSTRACT	c. THIS PAGE			Dr. Kevin C. Gross, AFIT/ENP
U	U	U	UU	95	19b. TELEPHONE NUMBER *(include area code)* 1 (937) 255-3636 x4558; kevin.gross@afit.edu

www.manaraa.com